The CLAS12 Drift Chamber System

M.D. Mestayer[a], K. Adhikari[f], R.P. Bennett[b], S. Bueltmann[b], T. Chetry[d], S.B. Christo[a], M. Cook IV[a], R.C. Cuevas[a], G.E. Dodge[b], T.A. Forest[c], G. Jacobs[a], T. Hartlove[b], T.B. Hayward[e], L. Kabir[g], S.E. Kuhn[b], D. McNulty[c], J. Newton[b], W.M. Taylor[a], L.B. Weinstein[b], V. Ziegler[a]

[a] *Thomas Jefferson National Accelerator Facility, Newport News, VA 23606*
[b] *Old Dominion University, Norfolk, VA 23529*
[c] *Idaho State University, Pocatello, ID 83209*
[d] *Mississippi State University, Mississippi State, MS 39762*
[e] *The College of William and Mary, Williamsburg VA 23185*
[f] *Hampton University, Hampton VA 23669*
[g] *University of California, Riverside, Riverside CA 92521*

Abstract

The CEBAF Large Acceptance Spectrometer at 12 GeV (CLAS12) is located in Hall B, one of the experimental halls at Jefferson Lab. The forward part of CLAS12 is built around a superconducting toroidal magnet. The six coils of the toroid divide the detector azimuthally into six sectors. Each sector contains three multi-layer drift chambers for reconstructing the trajectories of charged particles originating from a fixed target.

Each of the 18 planar chambers has two "superlayers" of six layers each, with the wires in the two adjacent superlayers oriented at ±6° stereo angles. Each layer has 112 hexagonal cells spanning a range from about 5° to 40° in polar angle. The six-layer structure provides redundancy in track segment finding and good tracking efficiency even in the presence of some individual wire inefficiency. The design, construction, operation, and calibration methods are described, and estimates of the efficiency and resolution are presented from in-beam measurements.

Keywords: CLAS12, drift chambers, tracking system. PACS: 29.40.Cs, 29.40.Gx

1. Forward Tracking System

The CLAS12 Forward Detector is constructed around a toroidal magnet consisting of six iron-free superconducting coils. The particle detection system consists of drift chambers to determine charged-particle trajectories, Cherenkov detectors for electron/pion separation, scintillation counters for flight-time measurements, and calorimeters to identify electrons and high-energy neutral particles. An overview of the CLAS12 subsystems and geometry may be found in the CLAS12 overview paper [1] in this volume. A schematic view of the torus magnet with drift chambers attached is shown in Fig. 1. The drift chambers are triangular boxes attached to the magnet cryostat. This assembly of the magnet and chambers is referred to as the "Forward Tracker".

The Forward Tracker can detect charged particles emerging from the target with momenta greater than 200 MeV at polar angles from roughly 5° to 40°. Particles with lower momentum are swept out of the tracking volume by the torus magnetic field. Because the coils of the torus magnet represent a "dead area" in which we cannot detect charged particles, we designed the chamber endplates and attached electronics to be as thin as possible. The resulting azimuthal coverage varies from 50% of 2π at 5° to 80% of 2π at 40°.

2. Drift Chamber System Conceptual Design

When the CLAS detector [2] was upgraded to become the CLAS12 detector, the drift chambers were re-designed. We kept many of the design concepts of the original CLAS chambers [3], but made improvements in a number of areas.

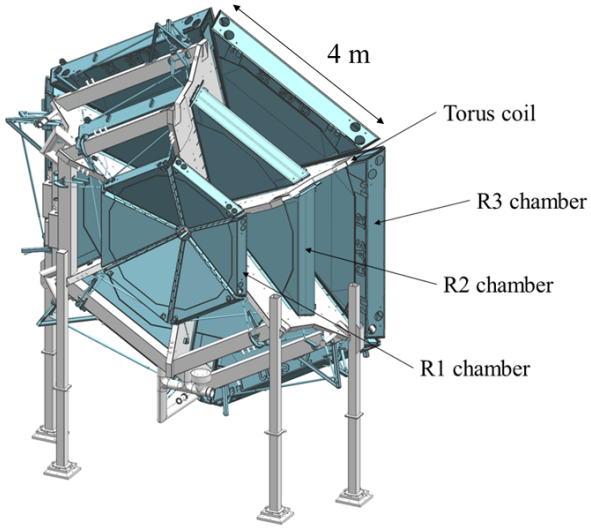

Figure 1: A model drawing of the torus magnet (light gray) with drift chambers (darker blue) attached. Note that the cable runs and gas lines have been removed for clarity. The largest chambers are approximately equilateral triangular solids with 4 m long sides and 0.8 m depth.

2.1. Physics Requirements for CLAS12 Forward Tracking

There are several broad areas of physics research that drive the design of the forward tracking system: spectroscopic studies of excited baryons, investigations of the influence of nuclear matter on propagating quarks, studies of polarized and unpolarized quark distributions, and a comprehensive measurement of generalized parton distributions (GPDs).

The cross sections for these processes are small, necessitating high-luminosity experiments. A variety of experiments rely on luminosities of 10^{35} cm^{-2}s^{-1} to achieve the desired statistical accuracy in runs of a few months duration. This is an order of magnitude increase compared to the previous CLAS detector.

The new kinematic range available to the CLAS12 experiment is characterized not only by smaller cross sections, but also by more outgoing particles per event, with those particles being emitted at larger momenta and smaller laboratory angles. A final state of a few high-momentum, forward-going particles (the electron as well as one or more mesons), combined with a moderate-momentum baryon emitted at large angles, is the typical event type that determines the specifications of the tracking system.

To cover as much of the hadronic center-of-mass region as possible, the CLAS12 Forward Tracker must provide tracking for charged particles emitted at polar angles from 5° to 40°. This is complemented by the angular coverage of the central tracking system, which covers polar angles from 35° to approximately 125°.

In addition to large acceptance, our experimental program requires small systematic uncertainties. To measure our electroproduction cross sections to an accuracy of a few percent, we must know the scattered electron's momentum to 1% and its angle to 1 mrad.

We need even better momentum resolution on the scattered electron (with momentum up to 10 GeV) to be able to identify particles by missing mass, an important technique in exclusive reaction studies. We performed tracking simulations assuming perfect knowledge of the drift chamber location (alignment) and perfect knowledge of the magnetic field, and assuming that the hit resolution in each of the drift chamber layers was 250 μm. These calculations are shown in Fig. 2, where we plot the estimated fractional momentum resolution (left axis) vs. momentum for different incoming angles (right axis) as a function of momentum.

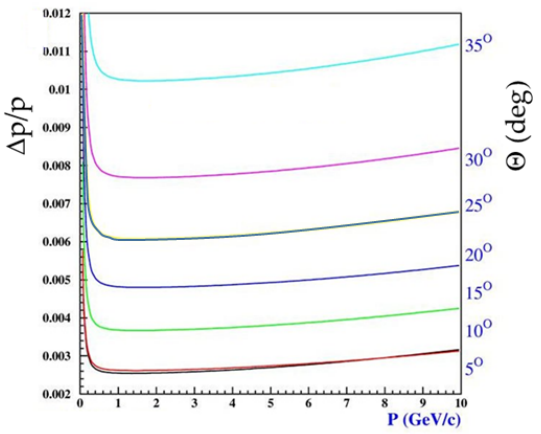

Figure 2: Estimated fractional momentum resolution plotted vs. momentum for different track angles.

These simulations led to our goal of $dp/p \approx 0.3\%$ for electrons emitted at small angles (7°) and high momentum (10 GeV). This requires very good position resolution per hit (on the order of 250 μm), very good positional alignment of the chambers

(≈50 μm), and very good knowledge of $\int Bdl$ on the order of 0.2%. These goals drive our calibration efforts; for more information see Section 8.

Table 1 lists the physics goals for the main CLAS12 program and the resulting drift chamber design specifications that will allow us to achieve these goals.

2.2. Drift Chamber Conceptual Design

Because the previous CLAS drift chamber system operated successfully for 15 years, we re-used many of the design concepts and most of the utility infrastructure, including parts of the gas mixing and handling system, the high voltage and low voltage systems, and many of the high voltage and signal cables. Refer to our article on the previous CLAS detector [2] and our article on the previous drift chambers themselves [3] for details.

We kept the same chamber layout as in CLAS: the forward-tracking system consists of three regions divided into six sectors as shown in Fig. 1; located just before, inside, and just outside the torus field volume, named Regions 1, 2, and 3 (and referred to as R1, R2, and R3), respectively. Each chamber has its wires arranged in two superlayers (SLs) of six layers each, with the wires in the two superlayers strung with ±6° stereo angles to each other. The cell structure is hexagonal, that is, each sense wire is surrounded by six field wires. This arrangement offers good resolution with very good pattern recognition properties.

The major difference compared to the previous design is that the chambers are located further downstream from the target and thus the drift cells cover a smaller solid angle than those in the previous CLAS chambers, allowing efficient tracking at higher luminosities because the accidental occupancy from particles not associated with the event is smaller.

2.3. Design Features

Table 2 lists the main design parameters for each region of the CLAS12 drift chambers. For the purposes of simulating track resolutions, we assumed that the position resolution of the individual drift cells would be 250 μm. The material budget for multiple scattering consists of about 0.02 radiation lengths before the R1 chambers due to an assumed 5 cm LH_2 target, the gas and low-mass mirrors in the Cherenkov counter, and the remainder of air. The total material in the R1, R2 and R3 chambers (each filled with a 90/10 mixture of argon/CO_2) and the intervening air also amounts to ∼0.02 radiation lengths.

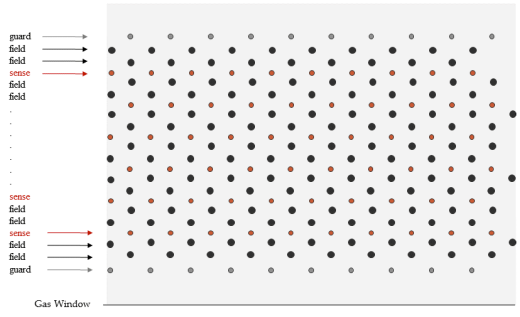

Figure 3: Wire layout for one superlayer; the view is a cut perpendicular to the wire direction.

2.3.1. Design Elements in Common with the Previous CLAS Chambers

The CLAS12 drift chambers share some design characteristics with the previous CLAS chambers:

- **Wire Layout**
  - "brick-wall" wire layout resulting in individual hexagonally shaped drift cells in a plane perpendicular to the wire direction;
  - sense wire layers are grouped into two "superlayers" of 6 layers each;
  - the "endplates" on the two sides of the chamber are tilted at ∼60° with respect to each other.
- **Chamber Body Design**
  - to maximize the active volume of the chamber, the "dead areas", e.g. the endplates and electronics boards, are kept as thin as possible;
  - because of the possibility of large eddy currents and resultant force on the endplates in case of the quench of our torus magnet, we again use non-conducting Stesalit 4411W endplates for our R2 chambers; ("Stesalit" is a trademark of STESALIT AG for a disordered epoxy-fiberglass composite product. See Ref. [3] on the previous CLAS drift chambers for more information.);

Goal	Physics Spec./Goal*	Design Specification
Measure Γ_v accurately	$d\theta < 1$ mrad $\sin\theta\ d\phi$ <1 mrad $dp/p < 1\%$	planar chambers $\pm 6^\circ$ stereo angle identical cells (each superlayer)
Select exclusive reaction; only one missing particle	*$dp/p < 0.3\%$ at 10 GeV	250 μm accuracy per cell chamber alignment < 100 μm
Small cross sections	Luminosity = 10^{35} cm^{-2}s^{-1} high efficiency	six 6-layer superlayers > 95% layer efficiency
large acceptance	$\delta\phi = 50\%$ at 5°	thin endplates

Table 1: Physics goals and the resulting physics and drift chamber design specifications.

	Region 1	Region 2	Region 3
Distance from target	2.3 m	3.5 m	4.9 m
Num. of superlayers	2	2	2
Layers/superlayer	6	6	6
Wires/layer	112	112	112
Cell radius (each SL)	0.78, 0.81 cm	1.14, 1.32 cm	1.87, 1.96 cm
Active time window	150 ns	325 - 1000 ns	750 ns

Table 2: Design parameters for the CLAS12 drift chambers.

- **Gas Choice:** 90:10 argon:CO_2 mixture. We operate at a gas gain of about 5×10^4.

Figure 3 is a schematic of the cell layout for a single superlayer. The wires are arranged in a "brick wall" pattern with one layer of guard wires, two layers of field wires, one layer of sense wires, another two layers of field wires, and so on, for a total of 2 guard wire layers, 14 field wire layers and 6 sense wire layers. The result is an hexagonal cell layout with each sense wire surrounded by 6 field wires.

2.3.2. Design Improvements Compared to the Previous CLAS Chambers

To improve the chambers' performance we made some important changes to the design:

- **Mechanical Design**
  - all chambers have the same, roughly equilateral triangular, shape;
  - the previous CLAS chambers were interconnected to each other (R1) or connected directly to the torus (R2). In the present chambers all of the wire tension is borne by the endplates and thus they can be independently mounted. The key to this improvement is the use of ultra-stiff endplate assemblies that obtain their stiffness by a flanged design;
  - all chambers are independent and self-supporting, allowing easy maintenance and repair. The chambers are attached to the torus cryostat using 6 independent rods arranged in a "ball-and-socket" linkage system, enabling the chambers to be moved out to their maintenance position and back to the operating position by turning one precision turn-buckle assembly.
- **Cell Design and Wire Layout**
  - For the previous CLAS detector, the ϕ resolution times $\sin\theta$ was about two times larger than the θ resolution. To have more equal resolution in the two angles, we doubled our stereo angle from 0 and 6° to $\pm 6^\circ$;
  - all chambers are planar, with the first superlayer (of 6 layers) tilted at a 6° stereo angle, and the second superlayer at a -6° stereo angle;
  - all wires within one superlayer are parallel to each other, thus every cell in one

superlayer is identical, making it easier to model and fit the distance-to-time response.

- **Wire Choice**
  - all chambers are strung with 30-μm gold-plated tungsten wire, considerably tougher and easier to handle than our previous choice of 20-μm wire;
  - the choice of the cathode ("field") wire is 80-μm gold-plated copper-beryllium, tougher and with better surface properties than our previous choice of 140-μm gold-plated aluminum wire;
  - Our choice of guard wire is 140-μm diameter, gold-plated copper-beryllium. These wires were strong enough that we pretensioned the chambers using only the guard wires; a simplification in the process.

Table 3 lists the advantages and disadvantages of the various design features.

2.3.3. Wire Diameter

One of the most significant design changes was the decision to use 30-μm diameter sense wire rather than the previously used 20-μm wire. This should make the chambers more resistant to wire breakage. The larger radius of the sense wires means that higher voltages will be required to achieve the same gas gain, see Section 7.3 for more details. Prototypes were built to study possible negative side-effects of the higher voltage operation, such as leakage currents on the circuit boards and/or higher rates of cathode emission from the field wire surfaces. No such effects were seen. We discuss the wire choice in more detail in Section 3.

3. Chamber Construction

3.1. Construction Overview

The three chamber types (called "regions", with "Region 1" abbreviated as "R1", etc.) share the same basic design elements simply scaled up in size by a factor of 1.5 for R2 relative to R1 and a factor of 2 between R3 and R1. Each chamber is a solid trapezoid in shape, with a pair of wire-supporting endplates that bear both the load of the wire tensions and the weight of all associated hardware. A representative chamber is shown in Fig. 4, with the component parts indicated. This particular drawing is of a R1 chamber, but all chambers have the same basic parts.

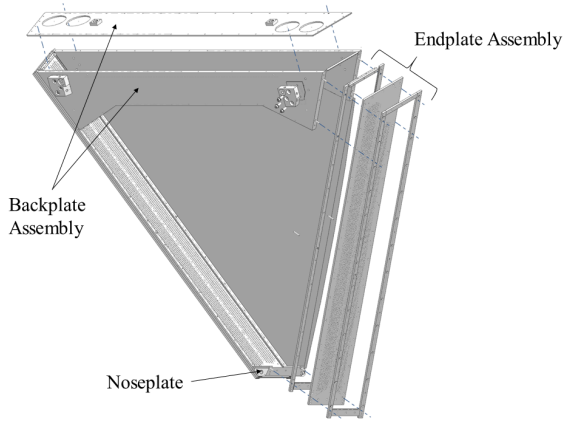

Figure 4: Assembly of a typical drift chamber (here a R1 sector) highlighting the common component parts in all CLAS12 drift chambers.

The chamber bodies were constructed from accurately machined plates (2 endplates, a "noseplate" and a "backplate"). The endplates themselves were an assembly of a main plate with precision-drilled holes to which we bolted and glued stiffener bars. In the case of R1 the main plate was aluminum and the stiffener bars were stainless steel; for R2 the main plates were non-conducting Stesalit material and the bars stainless steel, and for R3 the main plates were themselves an assembly of two thin steel plates with a foam interior. No additional stiffener bars were used for R3.

At the radially outward end of each chamber, a thick backplate was employed to maintain the relative alignment of the endplates, to stiffen the chamber against bending moments, and to provide a place to attach gas seals and fittings. At the radially inward end of each chamber, the endplates were connected together via a small joining piece called the noseplate. The hardware fabrication and placement was of critical importance to the dimensional accuracy of the chambers.

We used many of the same construction materials and procedures as we did in the previous CLAS chambers. See Ref. [3] for more details. For convenience, we repeat some of the descriptions in this article.

3.2. Construction Materials

To ensure a long working life for the chambers, care was taken to specify that all materials in con-

Design Feature	Advantages	Disadvantages
"All-wire design"	Little cathode emission	
Small Cells	Robust track-finding	Many wires to string
Hexagonal Cells	Minimum number of wires	Angle-dependence of time to distance
30 μm diameter sense wire	Resistant to wire breakage	Higher operating voltage
80 μm diameter field wire	Lower total wire tension	Higher fields on cathode wires
Opposite voltage for sense and field	Identical fields for all layers	More HV channels required
Self-supporting design	Easier maintenance	1 - 2 mm bowing of endplates

Table 3: Design features of the CLAS12 drift chambers.

tact with the gas volume were clean and "chamber safe" as defined in Ref. [4]. As previously, all construction was carried out in Class-10000 or better clean rooms.

The drift-chamber bodies were made primarily of aluminum (R1), Stesalit (an epoxy-fiberglass composite) (R2), or steel-clad structural foam (R3). See Section 3.7 for more discussion of the properties of Stesalit. The aluminum and steel parts were manufactured with machine oils and, as before, were subsequently cleaned with Micro-laboratory detergent from the Cole-Parmer Instrument Company. The Stesalit endplates were machined without any lubricating oils. Immediately prior to chamber assembly all parts were cleaned with detergent, then rinsed with deionized water and alcohol. The various wire attachment parts, feedthroughs and crimp pins, were cleaned in an ultrasonic bath with detergent and then rinsed in a second ultrasonic bath with deionized water.

It is important to avoid any outgassing into the chamber. As in the construction of the previous CLAS chambers, we used Shell Epon resin 826 mixed with Versamid 140, and Scotchweld varieties 210 and 2216 for chamber assembly and gluing of the feedthroughs. These mixtures have been studied extensively and found not to outgas significantly [5].

As before, the on-chamber gas tubing is mainly stainless steel, with some nylon tubing used in the gas manifolds. Special care was taken during all steps of construction and testing to ensure that no oils or silicones contacted any of the chamber materials.

3.3. Chamber Body Construction

The construction of the chamber bodies consisted of 3 main stages:

- receipt, inspection, and cleaning of parts;
- assembly of the main drilled plate and stiffener bars into a complete endplate, followed by insertion and gluing of the feedthroughs into the pre-drilled holes in the main plate;
- overall assembly of the endplates, noseplates, and backplates to make a chamber "box".

3.3.1. Inspection and Cleaning

After a visual inspection, we first cleaned the endplates and structural frame using a low residue laboratory degreasing solution and water rinse. We then performed a final cleaning using an ultrasonic bath of a laboratory-grade detergent solution. After two hours we rinsed with deionized water and then sprayed with methanol to aid drying. We cleaned the feedthroughs and other small parts with a similar procedure. In addition, the injection-molded parts were specified to be free of silicon mold releases.

3.3.2. Endplate and Chamber Body Assembly

We assembled the endplates on a table in the cleanroom. The various parts, the pre-drilled main plate and the various stiffener bars, were pinned and glued into place. Once the endplate assembly was finished, we inserted and glued feedthroughs into each hole. We took special care to use the minimal amount of glue required to provide a solid gas seal in order to prevent glue contamination inside the detector.

The feedthroughs are an assembly of a flared metal tube, a "trumpet", fitted into an injection-molded plastic feedthrough. The metal trumpets were produced on a screw machine, and delivered

to the injection molding factory. As with the original CLAS chambers, we specified the use of "Noryl" plastic reinforced with glass beads to make it stiffer. It is important to note that the surface conductivity of this glass-bead loaded composite is little affected by room humidities as high as 60%, in contrast to similar plastic strengthened with microscopic glass strands that performed poorly in high voltage stand-off tests in humid conditions.

Because our chamber endplates are not parallel, but oriented at $\approx 60^\circ$ with respect to each other, the wire position is determined by the concentricity of the feedthrough's trumpet and its placement and not by the concentricity or inner radius of the crimp pin; see Figs. 5 and 6.

This allowed us to design the crimp pin to maximize the crimp reliability and ease of use by using soft copper with a large enough inner diameter to be used for stringing all types of wire: sense, field, and guard. Using a thick-walled copper pin ensured a good crimp through a range of gap settings [6]. Having a single type of crimper required fewer re-calibrations; the soft copper made more secure crimps and the larger inner radius made stringing easier.

A schematic of the wire attachment schema is shown in Fig. 5. At this stage of endplate construction, the feedthroughs (part "2" in Fig. 5) were glued into place. Later, during the wire stringing phase, described in Section 3.5, the crimp pins (part "3") were fit into the feedthrough and crimped to hold the wire.

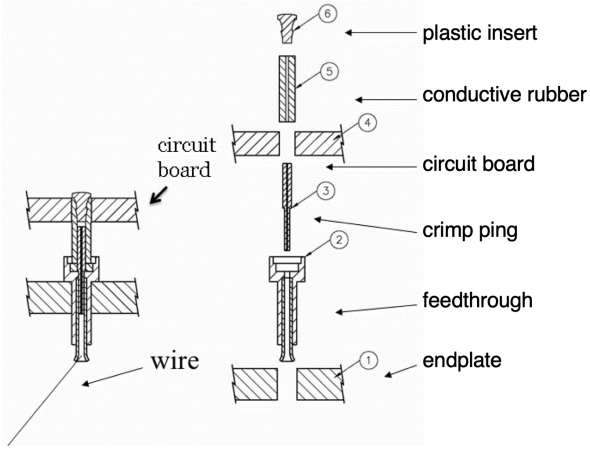

Figure 5: The collection of all parts used to physically attach a wire end to a chamber endplate and to provide an electrical connection to a chamber-mounted circuit board.

Once the endplates were complete with feedthroughs in place, we assembled the chamber box from the endplates, noseplate, and backplate using a variety of special-purpose fixtures. With the box held in its final configuration, the parts were bolted and glued into place using the special glues mentioned in Section 3.2. We used precision pinning extensively to achieve high dimensional accuracy.

3.4. Wire Choice

Our "thin endplate" design required minimizing wire tensions and thus the diameter of the wire. The real key to reducing wire tension is to make the field wires (which are much larger than the sense wires) as thin as possible and to make them out of low-density metal.

In general, designers have chosen very small diameter sense wires because they require lower operating voltages. The sense wire choice for all of our chambers, supplied by the Luma Sweden Company, is 30-μm diameter gold-plated tungsten. The previous CLAS drift chambers used 20-μm diameter wire for the sense wires. We decided to use the thicker 30-μm wire because it is significantly tougher, making it easier to handle without accidental kinking and less likely to break. As before, tungsten was chosen because of its durability, and we specified gold-plating because it is chemically inert.

We chose 80-μm gold-plated Cu-Be wire for our field wire and 140-μm gold-plated Cu-Be wire for our guard wires; both supplied by Little Falls Alloys. Cu-Be wire is very tough, is easily plated, and resists "flaking" of the gold plating. As mentioned, minimizing the field wire diameter is important because it means that they could be strung at lower tension than a thicker wire for the same gravitational sag. This minimizes the forces on the endplates that we wanted to keep as thin as possible to maximize the solid-angle of the sensitive area of the chambers.

The 80-μm diameter was chosen because it is the smallest diameter that will not initiate cathode emission at the surface. We designed for a gas gain of a few times 10^4; see Section 7.3.1 for further discussion of this. Under this condition, the electric field at the surface of the sense wires is $\approx$200 kV/cm and at the field wire surface is less than 50 kV/cm, preventing conditions that cause unwanted cathode emissions and a noisy chamber.

We note that our choice violated the "20 kV/cm rule", the conventional wisdom that a surface field greater than 20 kV/cm on the cathode wire would lead to a noisy chamber. Our own studies showed that there was no cathode emission below 50 kV/cm from any wire with good surface finish [7] . Each batch of wire was evaluated with our test device [8] to ensure that at operating field values there was no emission.

3.4.1. Wire Tensions

A basic principle of our drift chamber design is that each drift cell is a perfect hexagon in cross section. We used this geometrical constraint to determine the hole placement in the endplates. This design procedure assumed that wires are straight lines. Of course, real wires sag across the wire span due to gravity. To keep our perfect hexagonally shaped cells, we tensioned our three types of wires (sense, field, and guard) such that they sagged equally under their gravitational loads.

Our 30 μm tungsten sense wires, 80-μm Cu-Be field wires, and 140 μm Cu-Be guard wires had linear densities of 0.014, 0.042, and 0.129 g/m, respectively. To sag equally under gravity, they were strung at 20, 62, and 190 g of tension, respectively. In each chamber there were 12 rows of 112 sense wires, 28 rows of 112 field wires, and 4 rows of 112 guard wires for a total wire tension of 306 kg. This caused some bowing of our thin endplates. This bowing and the sagging of the wires themselves are discussed in the Section 8.3.1 on geometrical distortions.

3.5. Chamber Wire Stringing

Because all of the chambers have the same shape, differing only in size and some materials, we strung them all using the same basic method. They were gravity-strung using a similar methodology to that used when stringing the previous CLAS drift chambers. The detector box assembly was first mounted to a stringing fixture using the same ball-and-socket linkage system that was later used to attach the chambers to the torus magnet.

Under full wire tension, the endplates bow inward as much as 2 mm (see Section 8.3.1 for a discussion of this issue). Because of this bowing, it is necessary to pre-tension the chamber so that the endplates are bowed into their final state at the beginning of the stringing process.

We pre-tensioned the chambers by over-tensioning the 140-μm guard wires such that the total wire tension load was equal to the final, fully strung load. The over-tensioning was done using an adjustable spring attached to each guard wire. We then strung the field wires, starting at one end of the chamber. After stringing a "column" of 14 field wires, we reduced the tension on the associated guard wire to its nominal value, and crimped that guard wire. In this way, the total wire tension on the endplate (and its bowing) remained approximately constant through the stringing process.

We strung all chambers with the wires running vertically. The links were adjusted to place the feedthroughs in the upper plate vertically above the "partner" feedthroughs in the lower plate, which allowed gravity stringing.

The stringing technique began at the top endplate. The technician attached a small steel needle to the wire using a plastic tube with inner diameter only slightly larger than the radius of the needle. By inserting both the wire and needle into the plastic tube, a friction joint was achieved. The wire with needle attached was then threaded through the feedthrough in the upper endplate. The wire was then despooled and gravity acted to bring the wire close to the feedthrough in the lower endplate. A small magnet was used to pull the needle and wire through the lower feedthrough. The upper wire was then cut from the spool and a crimp pin was attached, crimped, and seated into its feedthrough. After the wire was attached at the upper end, the lower crimp pin was slid over the wire and seated into its feedthrough. Then weights were attached to the wire to set the proper tension, and the lower crimp pin was crimped, completing the process.

At the beginning of each shift, wires that had been strung on the previous day were tested in two ways:

- a continuity test checked that the wire made a good electrical contact from one feedthrough to its partner on the other endplate;
- a tension measurement was performed using an "oscillating wire" technique. A static magnetic field was established using large Helmholtz coils. A sine wave electric current was established on the wire being tested using a frequency-controlled AC power supply. The AC current could be varied in frequency. For a few-second interval, the Lorentz force on the wire caused it to vibrate and then during a few-second "voltage-off" period, the resulting in-

duced voltage was read out on an oscilloscope. In this way, we determined the resonant frequency of the wire.

If this frequency agreed within limits with a pre-calculated table of nominal frequency, the wire passed the frequency test. The tension limit for the longest wires (length greater than 3 m) was ±15%, while for the shortest wires (30 cm) the tension limits were +50% and −25%. Wires that failed either test were removed and re-strung.

Wires that wrapped around each other while being threaded through the chamber were a major contribution to stringing inefficiency. To avoid the wrapping problem, a machine was built to spool the wire through the chambers quickly and smoothly. As mentioned earlier, another important development was the design of a crimp pin that accepted both the tungsten and copper-beryllium wire types. This eliminated the need to use separate crimping tools, each requiring frequent calibrations. As a result, the average time to string a wire was less than 4 minutes.

After all wires were strung, a small amount of glue was applied to the glue well in the feedthrough to firmly fix the crimp pin in place. After this "potting" operation was done, the chambers were taken off of the stringing fixture and placed on stands on the floor for final continuity checks.

3.6. Region One Construction (Special Considerations)

The R1 chambers were designed and constructed through a collaboration of Idaho State University and Jefferson Laboratory. These chambers are located about 2 m from the target, before particles enter the magnetic field of the torus, and are thus key to good angular resolution.

As is seen from the generic assembly sketch of a chamber (see Fig. 1), the R1 chambers have a similar shape to the R2 and R3 chambers, differing in scale and in some material choices. Most notably, the endplates are constructed of aluminum with stainless steel stiffener bars.

The main challenges in the R1 construction and design came about because of the small wire spacing (8 mm between the sense and field wires). This increased the electrostatic attraction of neighboring wires if they were not perfectly and symmetrically placed, and it also made the physical act of stringing the wires more difficult.

Wires with opposite voltage are electrostatically attracted. If perfectly placed in a symmetric array the forces would cancel each other. However, the sense wires might be slightly misplaced and so they would feel a force which, if the tension were below a critical value, would increase and pull them further out, further increasing the force, and so on until the wire begins to oscillate and then spark. For our electric field configuration this critical tension was about 3 g, substantially below our nominal tension of 20 g.

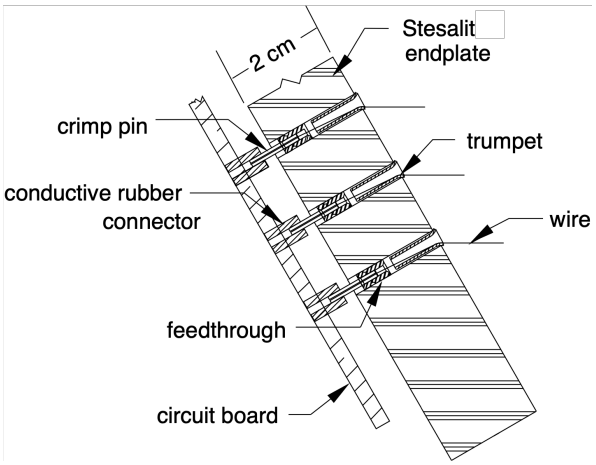

Figure 6: Schematic cross-sectional view of the R2 endplate showing the wire-positioning hardware.

3.7. Region Two Construction (Special Considerations)

The R2 chambers, which were designed and constructed by Old Dominion University in collaboration with Jefferson Laboratory, are the middle of the three drift-chamber packages. They track all charged particles in the magnetic field of the torus near the point of maximum sagitta. The six identical R2 sectors are approximately equilateral triangular boxes with 3 m sides. They are located at a radius of ≈3 m from the nominal target location.

The R2 chambers were designed with ultra-thin endplates that were thin enough to be wholly within the "shadow" cast by the torus cryostat; in other words, any track that does not strike the torus cryostat will enter the active fiducial volume of the R2 chambers. All chamber support hardware and electronics had to fit entirely within this shadow region. Figure 6 shows a slice through a chamber endplate

(R2 in this case) showing some of the wire positioning hardware and attachment of the electronics boards.

The R2 chambers have to operate in a magnetic field up to 2 T, and the chambers have to withstand any rapid changes in magnetic field, such as what might occur due to a magnet quench. The R2 endplates are constructed from 2-cm thick Stesalit 4411W, a disordered epoxy-fiberglass composite commonly used in wire-chamber construction [9], and known not to cause aging problems [10]. Using a non-conducting material eliminates any possible forces on the endplate due to eddy currents produced during a magnetic-field quench.

The Stesalit composite is not very stiff and, if not reinforced, would bend excessively under the load of wire tension. So, as in the case of the R1 chambers, the R2 endplates were a composite structure with stainless steel stiffeners. Figure 7 shows an assembly drawing of an R2 endplate.

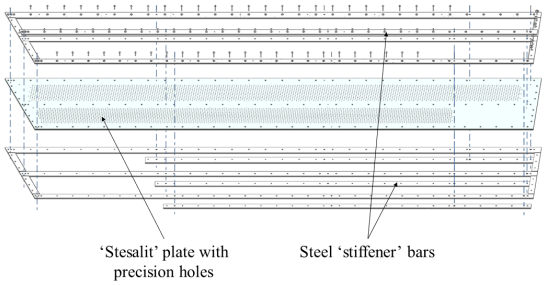

Figure 7: A R2 endplate assembly with its components highlighted.

The use of a non-conducting endplate also allows the trumpets that position the wires to be essentially flush with the endplates, rather than having to insulate the trumpets from the conducting endplates as in the other two Regions (see Fig. 6). This reduced the thickness of the inactive region by 1 to 2 cm.

3.8. Region Three Construction (Special Considerations)

The R3 chambers were designed and constructed at Jefferson Laboratory. They have the same shape as the other chambers but are larger, 4 m on a side, so the wires are as long as 4 m. To reduce the gravitational sag of these very long wires we strung wires with lengths between 0.6 and 0.8 of the maximum length at 30 g and the longest wires with lengths greater than 0.8 of maximum at 40 g, twice the nominal tension of 20 g.

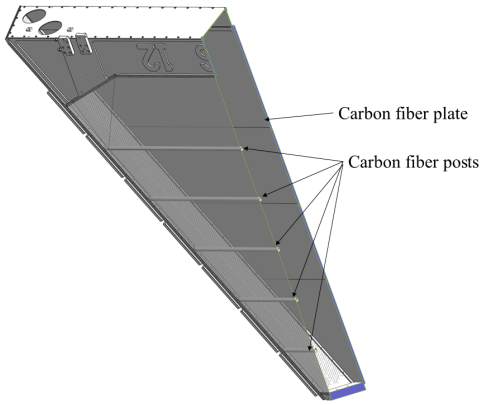

Figure 8: Assembly drawing of a R3 chamber showing the component parts and highlighting the carbon-fiber tubes at the entrance face and the carbon-foam composite plate at the exit, which supported the endplates against the wire tension.

Because these are the last of the tracking chambers, multiple scattering at the chamber entrance is less important than multiple scattering that occurs at a R1 or a R2 chamber. This allowed us to build a chamber in which the endplates were not supported only on their ends. See Fig. 8 for a depiction of the R3 box assembly.

At the entrance face we included 7 thin-walled carbon fiber tubes to span the gap and hold the endplates apart. At the exit face the endplates were coupled to a triangular carbon-foam-carbon composite plate that similarly supported the wire tension.

4. Drift Chamber Electronics

In this section we describe the drift chamber electronics: the on-chamber signal distribution and amplification boards, which we named Signal Translator Boards (STBs), the on-chamber High Voltage Translator Boards (HVTBs), and the off-chamber Drift Chamber Readout Boards (DCRBs).

On one endplate of each chamber is a set of HVTBs that distribute RC-filtered high voltage to the wires. Because there are three types of wire, (sense, field, and guard), we supply three different voltages to each HVTB board.

On the other side of the chamber are the STBs that support an individual Single Inline Package

(SIP) transimpedance preamplifier that is capacitively coupled to each sense wire since the sense wires are at high voltage. This preamplifier takes the small current pulse (as small as a few μA) and translates it into a voltage pulse with a transimpedance of 2 mV/μA. The signals (typically 10s to 100s of mV and 10s to 100s of ns duration) are transmitted down (17-pair) twisted-pair cables to our downstream DCRBs, which further amplify and discriminate the voltage pulses and then convert the leading edge to a digital time signal.

The drift chamber signal amplification and readout system thus consists of the following:

- chamber-mounted printed circuit boards with an amplifier for each signal wire; these are the STBs (one type for each superlayer);
- chamber-mounted printed circuit boards that distribute high voltage to all of the wires; these are the HVTBs (one type for each superlayer);
- a single 17-pair twisted-pair readout cable for each group of 16 SIPs;
- a 96-channel DCRB for each group of 6 cables (96 signal wires).

Table 4 gives a channel count for our chamber-mounted electronics components.

Component	Number
STB boards (6 types)	252 total
HVTB boards (6 types)	252 total
low voltage cables	252 total
high voltage cables	252 total
signal cables (17-pair)	1512
total signals	24192

Table 4: Electronic channel counts for the readout, high voltage, and low voltage systems for the drift chambers.

4.1. STB and HVTB: Installation and Use

The high voltage side of each chamber was tiled with 14 HVTB multi-layered printed circuit boards. These boards were designed to distribute three separate voltages to the sense, field, and guard wires, respectively. See Section 7.3 for a description of how we determined the operating values of the high voltage.

The board layout is shown in Fig. 9. Each high voltage cable is connected to a low-pass filter (with R=1 MΩ and C=1 pF) to eliminate any high-frequency noise from the supplies. The filtered power is then passed to the 4-layer printed circuit portion for distribution to the sense, field, and guard wires. To limit any potential high voltage breakdown, there is a 1 MΩ resistor for each sense wire.

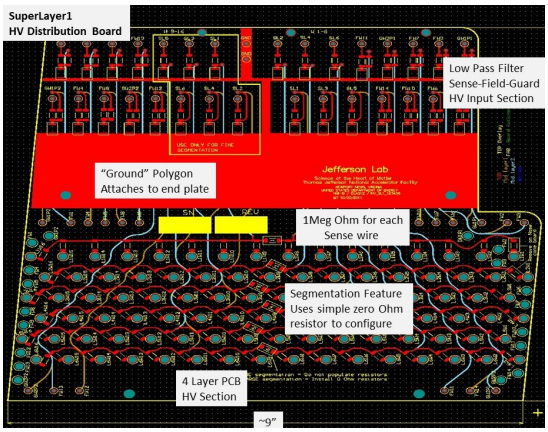

Figure 9: Board layout drawing for the High Voltage Translator Boards.

The signal side of each chamber was tiled with 14 STB multi-layered printed circuit boards. These boards were built in a 96-channel format that requires seven circuit boards for each superlayer (672 signals). The boards capacitively decouple high voltage from the signals, and then route the signals to the SIP transimpedance preamplifiers mounted on the boards. The amplified differential signals are then sent via 20-m long twisted-pair lines to the main CLAS12 readout electronics.

Figure 10 shows the layout of an STB board, including the trace routings from the capacitively coupled wire signal to the SIP and the placement of the SIPs into groups of 16 with the SIP outputs being routed to the 16-pin signal connectors. Also shown are the low voltage power traces with individual negative voltage regulators for each group of 16 preamplifiers. The negative voltage regulators were connected in isolation mode to provide +5 V DC regulated voltage to the group of 16 preamplifiers. The board shown is from a R1 chamber, which had the tightest wire and trace density.

The connections between the sense-wire crimp pins and the plated-through holes of the STB boards were made using short conductive-elastomer

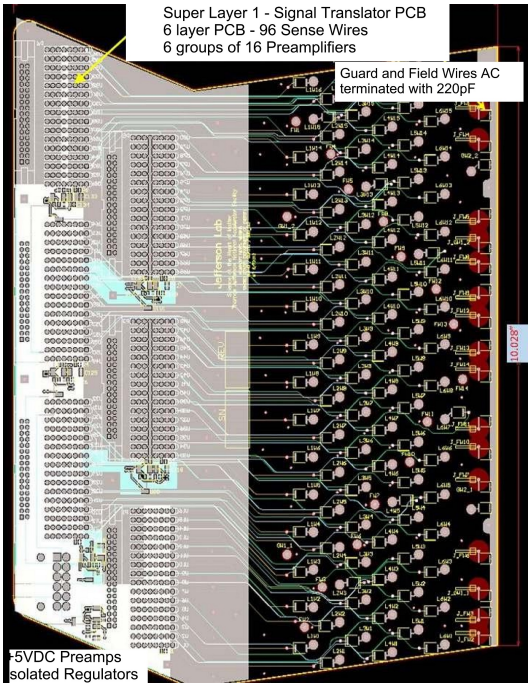

Figure 10: Trace routing shown on one of the R1 Signal Translator Boards.

tubes. This material consists of silver-plated and/or nickel-plated glass spheres embedded in a silicon-rubber matrix. These tubes pass through the plated-through holes and over the ends of the crimp pins, making the electrical contact between the wires and the circuit boards. A small plastic cap inserted into the end of the tube ensures good contact with the circuit board. This approach has the advantages of reducing the space needed for connections, preventing crimp pins from being pulled from the feedthroughs when disconnecting the boards from the wires, and reducing the cost compared to metal connectors. This detail is shown in Fig. 11.

4.1.1. Single Inline Package Preamplifiers

The heart of the STB board is an individually packaged Single Inline Package (SIP) preamplifier that was modified from the design of the previous CLAS detectors and included an epoxy resin encapsulation. The encapsulation of the components prevents component corrosion in a somewhat humid environment (relative humidities as high as 60%). These "CP01" preamplifiers provide the gain, dynamic range, rise time, low noise, and low power needed for the performance requirements. The

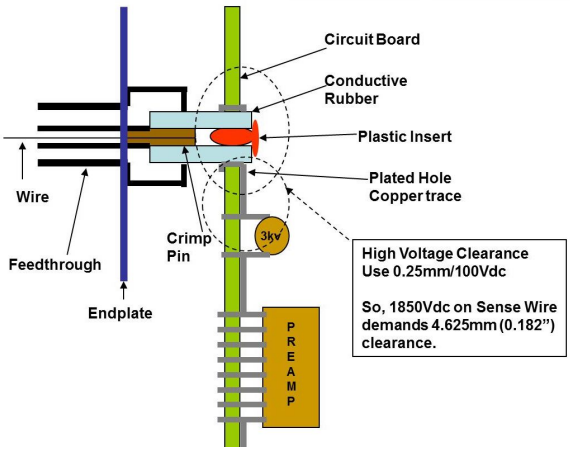

Figure 11: An assembly drawing showing how the crimp pin was inserted into the feedthrough and how the conductive elastomer tube fits over the crimp pin and inside the plated-through hole on the printed circuit board to make the electrical connection. Also shown is the signal path from the wire's crimp pin to the preamplifier.

CP01 is a transimpedance amplifier with a gain of 2 mV/μA and a rise-time of less than 10 ns. Each SIP operates at 5 V and draws about 13 mA. Figure 12 shows the design and specifications of the CP01 preamplifier. See Ref. [11] for the original design of this SIP preamplifier.

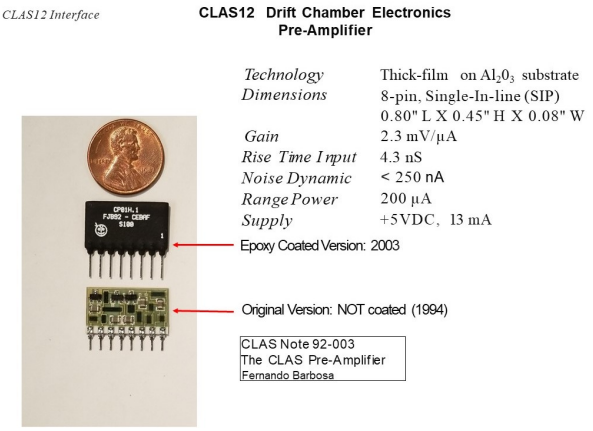

Figure 12: The CP01 preamplifier design and specifications.

Each group of 16 preamplifier output signals is routed to a 17-pair connector. Sixteen of the pairs are used as differential signal paths that are routed from the STBs to the DCRBs over individual cables consisting of 16 twisted pairs. We chose twisted-

pair readout because of its immunity to electronic noise. The cables are round-jacketed with a 0.025-in pitch so that the overall cable dimension is smaller than the standard 17-pair cable.

4.2. Off-Chamber Amplification, Time Digitization, and Readout

Our on-chamber preamplifiers send signals to the DCRBs, which provide another level of amplification, signal discrimination, adjustable threshold setting, time digitization, and readout.

4.2.1. Drift Chamber Readout Boards

The DCRB is a 96-channel board that is a combination post-amplifier, discriminator, and time-to-digital converter (TDC); it also has a trigger output path to provide track segment information for an online tracking trigger. Fourteen such boards are housed in a proprietary 9U, 160-mm depth, VXS form factor crate. The whole system consists of 18 such crates, one for each drift chamber. See Ref. [12] for more details.

These DCRBs are based on FPGA technology, and in addition to their primary function of amplification, discrimination, digitization, and readout, they are used in a simple "cluster-finding" algorithm to find track segment candidates with a latency of only hundreds of nanoseconds. For a more complete description of this please see our companion article on the trigger, Ref. [13].

To perform its time digitization task, the DCRB utilizes on-board synchronization to return the signal time relative to an input time signal from a Trigger Distribution Crate. Its design and architecture allows it to achieve the following performance metrics:

- DCRB Performance Metrics
  - Amplification: variable gain from $\times 10$ to $\times 30$ eliminates saturation
  - Time Digitization: accuracy better than 1 ns; exceeds DC specifications
  - Whole Crate Time Synchronization: through backplane, eliminates cables
  - Event Buffer Size: 500,000 signals
  - VME Transfer Rate: 200 MB/s
  - Maximum Trigger Rate: greater than 1 MHz
  - Dead-time: 32 ns
  - Scaler: 1 32-bit scaler per channel
  - Track Segment Finding: employs segment-hit dictionary in 32 ns bins
  - Track Segment Reporting: reports found segments to the next-level Track Finder

In addition to its primary functions of time digitization of DC signals and online track finding, the internal scaler functions allow the DCRB to be used in a stand-alone manner to efficiently monitor chamber operation during commissioning and testing.

4.3. Grounding Scheme

We use a single point grounding scheme, where the single point "ground" or zero reference is the CAEN high voltage power supply crates. Two return (ground) wires are used on every high voltage module output, and these ground wires are carried through to the HVTBs, which are grounded to the drift chamber endplates. The drift chambers themselves are insulated from the torus magnet through use of an insulating portion of the link mounting system. The off-chamber DCRBs are likewise not grounded to the chambers through the use of non-grounded twisted-pair signal cables. The low voltage power supplies were floating, supplying a plus and minus line to the +5 V DC regulators on the STBs.

5. Drift Chamber Utilities: Gas, Low Voltage, and High Voltage Systems

5.1. Gas System: Mixing, Monitoring, and Pressure Control

The chambers operate on a gas mixture consisting of 90% argon and 10% CO_2. Using precision mass flow controllers (MFCs), the gas is mixed and temporarily stored in large-volume buffer tanks. From these tanks it is delivered to experimental Hall B.

Argon is supplied via boil-off from a large, permanent dewar and CO_2 is supplied via boil-off from several standard industry high-pressure dewars. Two identical mixing systems are used to mix the gas to 90% argon and 10% CO_2 by mass using regulators and MKS G250 MFCs. The mixed gas is then stored at 100 psig in four large-volume ASME pressure vessels, also called buffer tanks. This large volume smooths out any minor fluctuations in the argon/CO_2 ratio. To control the gas

ratio, the thermal conductivity of the gas ratio is continually measured using Panametrics Thermal Conductivity Units (TCUs) and then matched to the thermal conductivity of a mixed gas calibration standard. Individual MFC flows are adjusted as needed if the gas mixture ratio changes. The mixed gas is supplied to the hall via two similar gas delivery systems, one for R3 and one for the combined flow through R1 and R2. We flow gas into the chambers at a rate of ∼2 - 3 volume exchanges per day; amounting to 36 l/min for the R3 chambers, 18 l/min for the R2 chambers, and 7 l/min for the R1 chambers.

MFCs and pressure regulators set the gas flow and pressure from the buffer tanks to the supply manifolds in the hall. In the hall, flow control for each individual sector is set using rotameters located at the supply manifolds. The gas flows into each detector at the nose and exits out of the backplate and into the exhaust manifolds. Since the gas volumes of R1 + R2 are about half the gas volume of R3, the R1 and R2 exhaust through one manifold and R3 exhausts through its own manifold. The exhaust manifolds are connected to pressure relief systems.

The drift chambers use thin, aluminized Mylar windows with a large surface area. Any over-pressure event could cause the windows to burst. Likewise, an under-pressure event could cause damage to the wires inside. Due to the potential of catastrophic damage to the detectors in the case of an over-pressure or under-pressure event, passive relief systems (bubblers) are installed on each exhaust manifold. In an over-pressure situation (i.e. high differential pressure between the exhaust manifold and atmosphere), the gas in the detector is vented out until the differential pressure falls to a safe level. In an under-pressure situation (i.e. low differential pressure between the exhaust manifold and atmosphere), air is sucked into the exhaust manifold until the differential pressure increases to a safe level. Each of these high-flow differential pressure relief systems consist of 3 parts: an oil-filled over-pressure bubbler, an oil-filled under-pressure bubbler, and an empty oil trap, all filled with high-purity mineral oil. The oil trap is connected to the exhaust manifold, while the over- and under-pressure bubblers are connected directly to the oil trap. This prevents contaminating the exhaust manifolds with oil. Additionally, each of the 3 parts contain baffles to remove oil droplets from the gas passing through the unit.

Figure 13 shows a schematic of the gas delivery system and a snapshot of the control panel for monitoring the state of the system. The figure illustrates a typical running condition where water infiltration is less than a hundred ppm and oxygen infiltration less than a few hundred ppm. These levels should negligibly affect signal size; for example, see Ref. [14] for a discussion of the effects of Oxygen contamination.

5.2. Low Voltage System

We reused the CLAS low voltage power supplies; see Ref. [3] for details. The supplies are remotely programmable and monitored. The on-chamber preamplifiers require 6 V and 18 A per chamber to the STB regulators, (a total of 1344 preamps per chamber).

We isolated the low voltage from ground loops by using local voltage regulators on the preamplifier interface boards (STBs). The segmentation of the low voltage distribution cables is based on 32 preamplifier channels per supply cable. Each of the supply cables is fused for over-current protection based on the average current draw of 32 preamplifiers.

We designed our low voltage system (supplies, fusing, cables, and control system) to be as robust and maintenance-free as possible. To minimize the damage to the tracking system in the event of a failure such as a shorted preamplifier, we built in fine segmentation with only 32 preamplifier channels per supply cable. In the event of a short circuit that causes a fuse to blow, a simple, external cable disconnect will reduce the size of the affected area to 16 signal wires without the need to access the chambers.

Figure 14 shows a schematic of the low voltage supply system and a snapshot of the control panel for monitoring the state of the system.

5.3. High Voltage System

As in the case of the low voltage system, we designed our high voltage system (supplies, distribution boxes, cables, and control system) to be as robust and as maintenance-free as possible. We reused our CAEN system 527 high voltage supplies with somewhat finer segmentation than our previous system, consistent with our total channel count dropping from 34000 to about 24000. To minimize the damage to the tracking system in the event of a failure such as a broken wire, we built in very fine

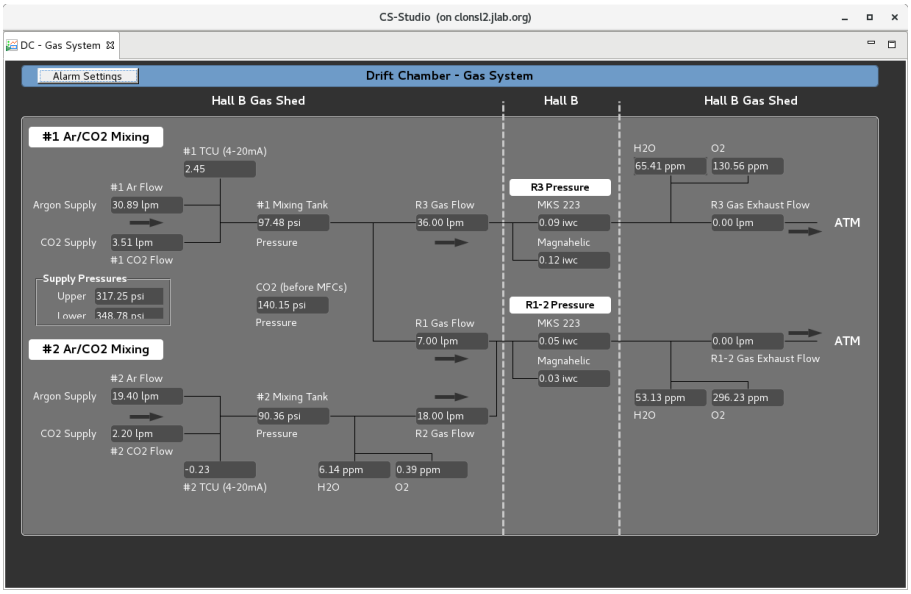

Figure 13: A schematic of the drift chamber gas system showing key control and monitoring points.

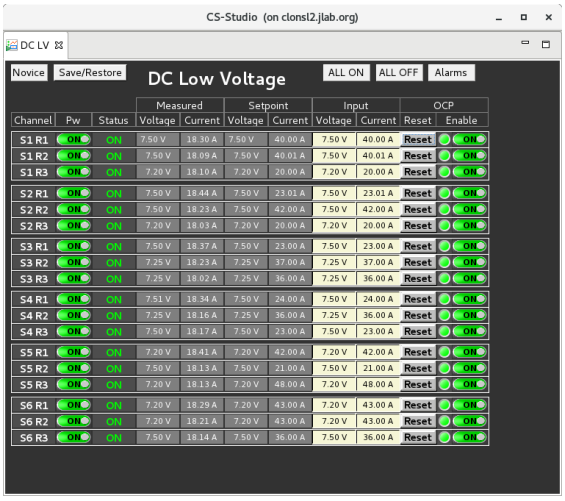

Figure 14: A schematic of the low voltage control and monitoring scheme.

segmentation. Each individual high voltage channel powers a variable-sized group of wires: a 48-wire group for wires in the small-angle region, a 96-wire group in the middle-angle region, and a 192-wire group at large angles.

In the event of a failure (e.g. a broken wire) that results in a trip of a single HV channel, we can further reduce the size of the affected area from the whole group (48, 96, or 192 wires) to a smaller grouping of 48 wires by an external cable disconnect without the need to physically access the chambers themselves.

The high voltage supply and distribution system consists of the following:

- a crate-based high voltage power supply with 36 independent high voltage channels for each drift chamber (1344 signal wires each). Of these 36 channels, 16 supply positive high voltage to the sense wires, 16 supply negative voltage to the field wires, and 4 supply positive voltage to the guard wires;
- a series of two distribution boxes that distribute the high voltage from the supply channels to variable-sized groups of wires, with the group size being 48 wires (for small angle wires) to 96 (intermediate angles) to 192 (large angles);
- on-chamber printed circuit boards that distribute high voltage to all of the wires; these are the HVTBs.

Figure 15 is a schematic of the high voltage supply system and a snapshot of the control panel for monitoring the state of the system. There are 648 individual remote-controlled high voltage channels shown. In this particular snapshot, two channels are colored red (or darker) to indicate a high voltage trip for the sense and field wires for Sector 2, R2, superlayer 1, wires 32-48. The fact that the adjacent sense and field wire channels both tripped indicates that there was an over-current condition for this group of wires with current probably flowing from field to sense wire; i.e. likely over-current in the chamber itself. This happens occasionally when the beam is mis-steered, causing higher than normal background radiation.

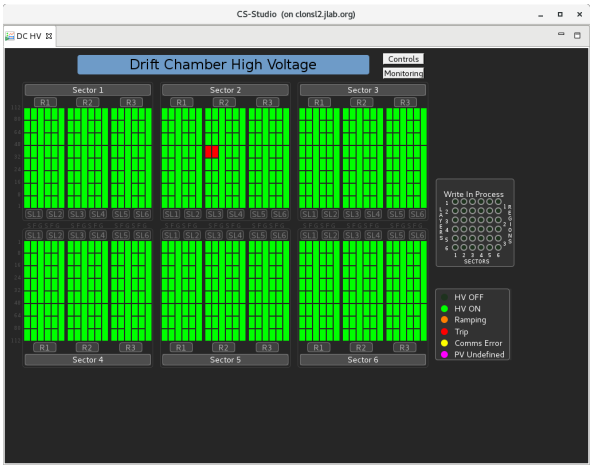

Figure 15: A schematic of the high voltage control and monitoring scheme, showing the 648 remotely controlled channels. The red (darker) cells in R2 Sector 2 indicate a high voltage trip.

6. Pre-Commissioning and Installation

In this section we describe the procedures that took place after chamber stringing was complete in order to get the chambers ready for installation and to install them in Hall B.

6.1. Electronics Installation and Turn-on

After the chambers were strung and went through a mechanical quality check to insure that all wires were intact and properly tensioned, we installed the on-chamber electronics boards, using the following procedures:

1. "daisy-chained" the field wire crimp pins so that a single high voltage cable could power two rows of field wires (32 wires);
2. physically positioned the boards so that their plated-through holes aligned directly above the sense wire crimp pins, and attached the boards to the chamber with screws;
3. electrically connected each sense wire crimp pin to each plated-through hole using a conductive elastomer tube that fit over the crimp pin and also contacted the plated-through hole on its outer radius.

A sketch of the process of attaching the circuit boards to the chambers is shown in Fig. 16.

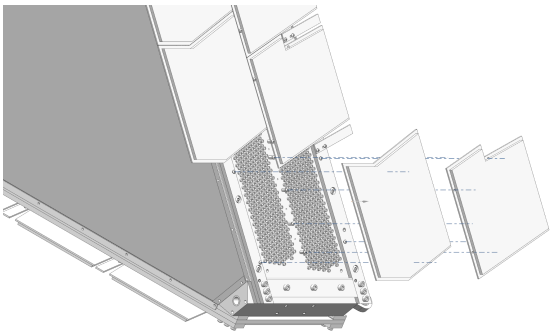

Figure 16: A sketch showing an on-chamber STB board being mounted.

Now the chamber was ready for "burn-in" and "pre-testing".

6.2. Burn-in and Pre-testing

When drift chambers are first turned on, they typically draw fairly high "dark" currents, even at low voltages. The standard procedure is to slowly raise the high voltage, wait for a certain time period during which the current subsides and raise the voltage again, and so on. For our chambers, the typical time period was an hour and the typical voltage step was 75 V. For comparison, 100 - 120 V is approximately the "doubling voltage" of our chambers (the voltage step that increases the gain by a factor of two). The total time of "burn-in" for each chamber varied from one to three days. Visual observation of good signals on an oscilloscope completed the pre-testing.

6.3. Installation and Survey

The chambers are attached by ball-and-socket joints to rods that are attached on the other end by

ball-and-socket to the toroidal magnet frame. After the initial installation, the chambers were moved to an approximate working location. Then, with the survey crew's information, the chamber location was fine tuned by lengthening or shortening the rods with fine-pitch screw adjustments. In this way the final chamber positioning was performed with sub-millimeter accuracies as determined by the survey group's laser positioning system.

The installation of 18 chambers took months to accomplish and the survey crew's work was hindered at times by obscured views of some of the fiducial marks on the chambers. We checked and updated the survey information with a later "straight-track" zero-field alignment run and analysis procedure (see Section 8.3 for details of the alignment). Although most of the alignment numbers were verified to sub-millimeter accuracy, there were a few parameters that were off by as much as 2 mm.

Of particular note regarding the "rod and ball-and-socket" mounting scheme:

- by design, changing the length of any or all of the six links will move the chamber in position and/or angle but will not apply stress to the chamber;
- once installed and surveyed, the chamber can be moved out to maintenance position by changing only one of the link lengths;
- this "one link" motion is reproducible to sub-millimeter accuracy, reducing the time and manpower required for maintenance and repair. In a matter of 8 hours, a chamber can be moved to "maintenance position", repaired, and moved back to installation position without the need for a re-survey. Figure 17 shows a single chamber in its maintenance position.

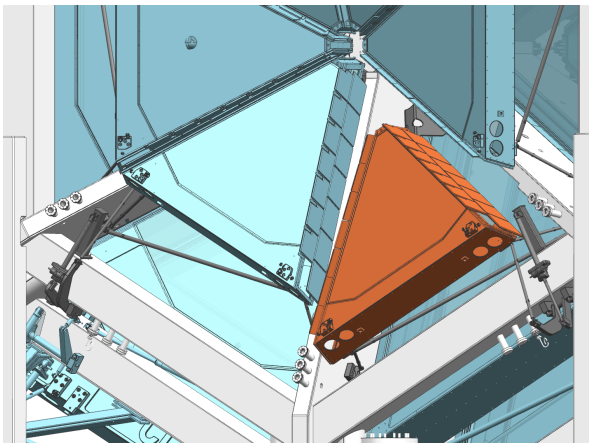

Figure 17: A view of the drift chambers mounted onto the torus magnet, with one R1 chamber moved out to its maintenance position.

7. Chamber Operation and Performance Monitoring

7.1. Choice of Gas

The main requirements for the chamber gas were that it have reasonably low multiple scattering, allow for reasonable gas gains, have high drift velocities in order to reduce the random background expected from Møller electrons and target-generated X-rays, and be inexpensive because of the large volume of the chambers. Also, safety considerations motivate the use of a non-flammable gas mixture. Additional concerns about small gas leaks and the proximity of many photomultiplier tubes argued against helium mixtures. Ultimately, a 90% argon - 10% CO_2 mixture was employed for several reasons: the gas has a fairly high saturated drift velocity (>5 cm/μs), and it has an operating voltage plateau of several hundred volts before breakdown occurs. The 90%/10% mixture provides good efficiency and resolution, and reasonable collection times.

7.2. Selecting the Proper Operating Voltage

In this section we discuss our operating voltages and how they were determined. First, we discuss how we divided the total voltage between our sense, field, and guard wires in order to mimic a cell layout with an infinite number of layers, achieving a situation in which all wires, regardless of layer, have the same gain. Then we discuss our choice of the total sense to field wire difference in voltage, including the resulting gas gain and efficiency.

7.2.1. Dividing the Total Voltage Between Sense, Field, and Guard Wires

We ran our chambers with a mixed voltage scheme: positive high voltage on the sense wires, negative voltage on the field wires, and positive voltage on the guard wires. This mixed-voltage scheme has several advantages over a scheme in

which the field wires, for example, are held at ground potential:

- fewer field lines run from the sense wire to the endplate, which is grounded. This reduces the likelihood of producing a "Malter effect" [15] in which an accidental source of cathode emission (due to an insulating contaminant on the endplate, for example) causes a self-sustaining discharge;

- the sense-to-ground potential and the field-to-ground potentials are smaller, decreasing surface electric fields on the on-chamber circuit boards.

In addition, by selecting the values of the sense, field, and guard wire voltages such that the net charge on all wires is zero, we create potential distributions that mimic an infinite grid of cells, where the gain on any wire is the same as any other, regardless of whether it is the first, last, or middle layer.

This optimum condition is reached when the sense voltage is twice the field voltage (and opposite polarity). This is because we have twice as many field wires as sense wires and all field lines that originate on a field wire land on a sense wire.

The guard wire voltage was then chosen so that the total charge on all wires is zero. If we have a nearby ground plane due to the metallized gas window, in general there will be an induced surface charge on the window that will affect the surface charge on the wires and thus the gain of the nearby wire layers. However, if the net charge on all wires is zero, then there is no net flux of electric field through the gas bag and thus the net charge on the gas bag is zero. In this way all of the wires have the same gain, regardless of layer. See Ref. [16] for a discussion of these issues.

We used the drift chamber design program GARFIELD [17] to determine the voltages necessary to achieve the condition of net charge equal to zero. The resulting ratio of voltages from sense to field to guard wires is 1 : -1/2 : 5/14.

7.3. Determining the Operating Values of the Discriminator Thresholds and High Voltage Settings

We set the discriminator levels in the DCRBs to reduce the accidental hit occupancy (with no beam) due to electronic noise to be less than about 1%. Since the electronic noise was generally proportional to wire length, we had less electronic noise on the smaller R1 chambers. Using this criterion, we set the thresholds to 30, 45, and 45 mV, respectively, for R1, R2, and R3. Once we set the discriminator thresholds, we performed a high voltage efficiency scan.

We determined the layer efficiency using the "excluded layer" method. In one superlayer (of six layers) we found track segments by our usual fitting method, but ignored the data from a pre-selected layer. We then projected the track segment through that layer and determined whether or not the indicated wire (or an adjacent one) had a good hit. We raised the sense to field wire potential in steps of 75 V and analyzed the data. We set the operating value for the high voltage at the point at which the layer efficiency (the probability that a track passing through a layer will fire at least one wire) equaled or exceeded 97%.

7.3.1. Operating Voltage and Gas Gain

The gas gain varies exponentially with the total sense to field wire voltage difference, with a doubling voltage of about 100, 110, or 120 V, respectively, for R1, R2, and R3. During our fall 2018 run, we ran with sense - field wire voltage differences of 2100, 2325, and 2475 V, respectively, for R1, R2, and R3. We calculate that our total gas gain is approximately 2.7×10^4, 3.7×10^4, and 4.4×10^4, respectively, for R1, R2, and R3.

7.4. In-Run Performance Monitoring

The CLAS12 detector records 10,000 - 20,000 events/s during a typical experiment. It is important that the experimenters who are overseeing the data-taking be quickly aware of any equipment malfunctions.

Our first level of monitoring comes from our hardware alarms; see Section 5 to see images of the control panels for our gas system and power supplies. Should these malfunction, an alarm is instantly shown on an alarm summary screen with Graphical User Interface (GUI)-driven information on the lower-lying hardware monitoring screens. An experimenter is thus able to detect an alarm, and in most cases, reset the alarming supply, within minutes.

Our second level of monitoring comes from online accumulating histograms. Of these, the most important are our so-called "Occupancy Plots", which

are simply histograms of wire hits plotted vs. wire number and wire layer (summed over six superlayers in each sector). Malfunctions show up as depleted areas on the plots.

Figure 18 shows a histogram of wire hits in a grid of layer (1 - 36 on the vertical scale) vs. wire number for each of the six sectors. A R1 chamber contains layers 1 - 12, a R2 chamber layers 13 - 24, and a R3 chamber layers 25 - 36. The horizontal axis shows the wire number in each layer (1 - 112). At a glance, one can inspect our 24,000 wires and determine that >99% of wires are functioning properly. A few areas of inefficiency are visible in the upper middle graph, corresponding to two areas in which the high voltage was disconnected to stop excessive current draw.

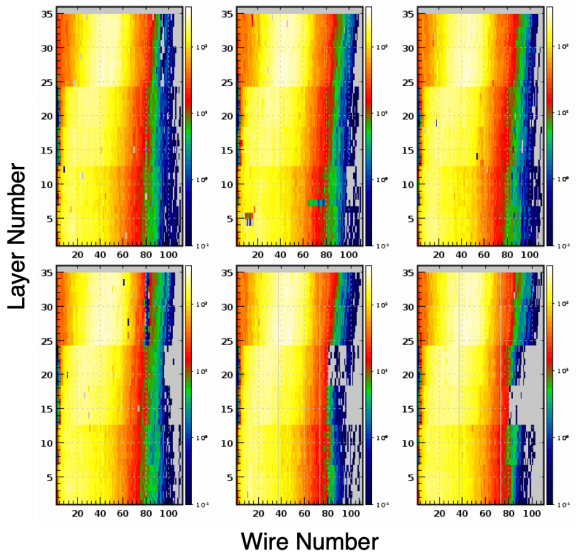

Figure 18: An "occupancy plot" showing the number of wire hits accumulated over many events for all six sectors. A few malfunctioning wire groups can be seen in the upper middle graph.

8. Drift Chamber Calibration Procedures

Forward-going (5° to 40°) tracks are fit to wire hit positions in each of the 36 wire planes. These hit positions are not simply the wire location, but a calculated position: a distance-of-closest approach (DOCA) to the wire, derived from the hit wire's recorded TDC value.

Here we discuss our procedures to calibrate our TDC to DOCA conversion tables, as well as specialized alignment procedures we undertook to most accurately determine the wire positions themselves. Finally, we close with a summary of our magnetic field measuring and modeling procedures.

8.1. Time-to-Distance Calibration

The drift chamber Time-to-Digital Converters (TDCs) measure time. These TDC units are part of our overall DCRB boards and have an intrinsic resolution of 1 ns or better, too small to be relevant to our overall time-to-distance calibration.

First, the digitized time is corrected for a number of effects, and this corrected time is converted to a DOCA, by a pre-calculated time-to-distance function. In this subsection we explain the time corrections, the function used to calculate time as a function of DOCA, and how we calibrate the parameters of this function.

8.1.1. Time Corrections

The drift time is the elapsed time between the time that the particle traversed the wire cell and the time that the released gas ions (electrons) reached the sense wire. The drift time is given by the following expression:

$$t_{drift} = t_{tdc} - t_{start} - t_0 - t_{flight} - t_{prop} - t_{walk}, \quad (1)$$

where t_{tdc} is the raw time measured by the TDC, t_{start} is the event start time (the time at which the triggering particle left the target), t_0 is the fixed-time (cable) delay for the wire, t_{flight} is the flight time of the particle from the interaction vertex to the wire, t_{prop} is the signal propagation time along the wire, and t_{walk} is a shift of the recorded hit time to larger values that depends on the ion density of the track (velocity or β-dependent) and the distance of the track to the wire. With a trigger based on detecting an electron in the CLAS12 detector, the event start time is given by the Forward Time-of-Flight system's [18] counter time for the scattered electron, corrected for the calculated flight time of this electron from the beam-target vertex.

As indicated in Eq. 1, the fixed-time delays for each wire must be known in order to determine the drift times. To determine this t_0 value, we produced a histogram of the following quantity for all hits used on tracks: $(t_{tdc} - t_{start} - t_{flight} - t_{prop} - t_{walk})$. This produced a characteristic plot of a drift chamber signal on a flat background from out-of-time tracks. A fit to the leading edge (a sigmoid with linear extrapolation) returned the value of t_0.

8.1.2. Time-to-Distance Functional Parameterization

After correcting the raw TDC, we needed to convert the corrected time from the wire to an estimated DOCA. Note, we refer to two variants of DOCA: one is "TRKDOCA", which is the fit value of the track's closest approach to the wire and the other is "DOCA", which is calculated from the measured time for the wire hit.

A best fit to a scatterplot of TRKDOCA vs. time should define the time to distance function of the drift cells. However, several factors complicate this analysis. First, the TRKDOCAs obtained from the fitted tracks are biased quantities since the initial estimate of the drift-velocity function is used in the track determination. Moreover, the drift cells are not circular, as the analysis implicitly assumes, but are hexagonal, leading to angle-dependent corrections. Also, the R2 chambers are in a region of high and spatially varying magnetic field. Finally, the different ionization densities of the tracks from particles with different velocities leads to substantial time-walk corrections for tracks near the wire. Each of these points is discussed in this section.

Figure 19 shows the isochrone contours and electric-field lines for a representative R3 and R2 cell. Note that the contours are circular close to the wire but become hexagonal near the outer boundaries of the cell. This illustrates the necessity of knowing the entry angle of the track in order to determine the drift distance to the sense wire from the measured drift time.

8.1.3. Distance-to-Time Function Parameterization

In the CLAS detector, the drift distance was parameterized and fit as a function of drift time [19]. In contrast, for CLAS12, we have instead chosen to parameterize the time as a function of distance. This is a more natural description of the drift chamber signal for several reasons:

- the maximum drift distance is given by geometry (the distance from a sense wire to the nearest field wire) and so it is fixed;
- the drift velocity is a function of electric field strength, so the point of minimum velocity is located at the point of minimum field (and thus the inflection point on the t vs. x curve). This inflection point of the curve occurs at a definite value of distance within the cell and not at a definite value of time;
- the time walk due to finite ionization is naturally parameterized as a function of distance and not as a function of time;
- a time correction for wires in a magnetic field (which scales like the square of the magnetic field strength B^2) can simply be added to the nominal functional form.

This single functional form is used to fill two tables:

1. a table of time indexed by distance for use in the simulation;
2. a table of distance indexed by time for use by the track reconstruction code.

8.1.4. Choice of Mathematical Form for the Distance-to-Time Function

We use a 4th order polynomial to model the distance to time relationship,

$$t(x) = ax + bx^2 + cx^3 + dx^4, \qquad (2)$$

where t is the time in ns and x is the distance in cm. By the use of simple calculus we convert the parameters a, b, c, and d to equivalent parameters that have a physically intuitive meaning.

8.1.5. Physical Constraints on the Drift Velocity Function

Inspection of Fig. 19 reveals that for tracks near the outer edge of the cell, the first arriving ions follow the electric-field line from the field wire to the sense wire, independent of track entrance angle. The corresponding drift time is referred to as $Tmax$ and occurs when TRKDOCA is at its maximum value, called $Dmax$.

A second constraint is that the velocity near the wire is the "saturated drift velocity" for our gas mixture of 90% argon - 10% CO_2. We call this parameter V_0.

A third constraint is imposed by the fact that there is a definite point along a line from the sense wire to a neighbor field wire at which the electric field is a minimum. This implies that this is the point of minimum velocity and is thus an inflection point. This occurs at a value $r = (x/Dmax) \approx 0.64$ and the drift velocity at this point is termed V_{mid}.

In summary, the function coefficients are constrained as follows:

1. $t(x)$ must equal $Tmax$ when $x = Dmax$;

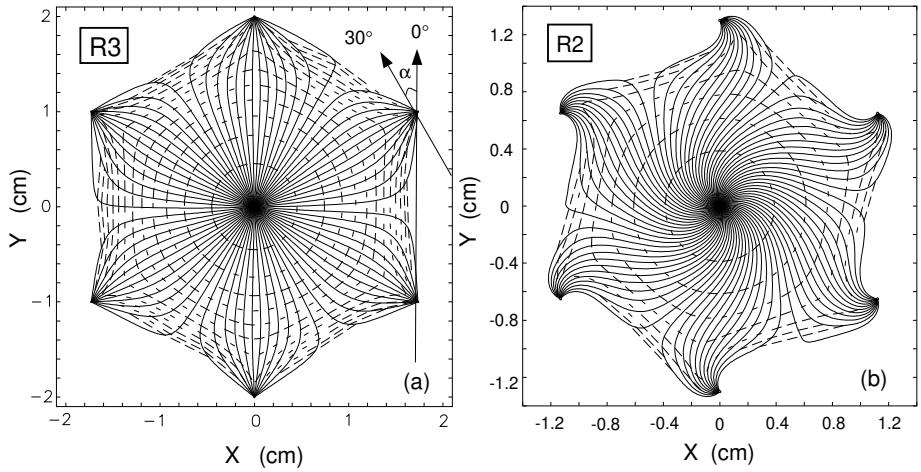

Figure 19: Plot of electric-field lines and equal-time isochrone contours (100 ns interval) for a 90% argon - 10% CO_2 gas mixture for (a) an R3 drift cell where two rays are drawn highlighting two different track entrance angles of α = 0° and 30°, and (b) an R2 cell that was assumed to be located within a uniform 1 T magnetic field pointing into the page.

2. the drift velocity near the sense wire ($x = 0$) must equal the saturated value, V_0;
3. the function has an inflection point (a minimum in velocity) at the point in the cell with the lowest electric field strength. From the geometry of our cells, this occurs at a distance of $\approx 0.64\ Dmax$; and
4. the velocity equals V_{mid} at the inflection point.

In this way we convert our original parameters, a, b, c, and d to the physically meaningful parameters $Tmax$, V_0, r, and V_{mid}, where r has the value 0.64 (the fractional distance at which the inflection point occurs), which can in principle also be varied. These secondary (physically meaningful) parameters are the ones that are used by our distance-to-time calibration program.

In particular, we can compare our results for V_0 (the drift velocity at high electric field strength ($\geq$1000 V/cm)) and V_{mid} (the drift velocity at the point of minimum electric field strength ($\approx$ 250 V/cm)) with published results [20]. This is helpful in the early stages of calibration.

8.1.6. Dependence of Distance-to-Time Function on Local Angle

The preceding was the derivation of the formula for time as a function of drift distance for tracks with a local angle $\alpha = 30°$ and for magnetic field B=0. Tracks with local angle α less than 30° have a maximum distance that is smaller than $Dmax$.

Figure 20 provides an illustration of the local-angle dependence of distance vs. time. When the time is equal to $Tmax$ the distance is equal to the largest value for the local angle, namely, $Dmax_\alpha$. Also note that by simple geometrical reasoning, $Dmax_\alpha = Dmax \cdot \cos(30° - \alpha)$. We assume that at times less than $Tmax$ and distances less than $Dmax$, the calculated distances still vary linearly as $\cos(30° - \alpha)$. This angle dependence is built into our functional form.

Figure 19 shows a 0° track and a 30° track, both at maximum distance from the sense wire. They will produce a signal hit with the same time $Tmax$ even though their DOCA differs by a factor of $\cos 30°$. If $Dmax$ is the distance from sense to field wire (and the maximum DOCA possible for a 30° track), then $Dmax \cdot \cos(30° - \alpha)$ is the maximum DOCA for a track with local angle α. Call this distance $Dmax_\alpha$. We derived the function for time vs. distance for a particular local angle α by assuming the same functional form as for $\alpha = 30°$ but with a different coefficient d, which satisfies the constraint that $F(Dmax_\alpha, \alpha) = Tmax$.

Using this constraint, we can solve for d_α in terms of the coefficients a, b, c, and d, yielding the following:

$$d_\alpha = \frac{Tmax - a\ Dmax_\alpha - b\ Dmax_\alpha^2 - c\ Dmax_\alpha^3}{Dmax_\alpha^4}. \quad (3)$$

Using this formula for d_α we can derive the time

as a function of distance and local angle α as shown in Fig. 20. See, for instance, the upper-left subfigure, which shows the time as function of distance for 5 different angles between 0° and 30°, equally spaced in $\cos(30^\circ - \alpha)$. Note two things:

1. for each angle α the time is $Tmax$ at $Dmax_\alpha$;
2. the distances for a given time vary with angle α as $\cos(30^\circ - \alpha)$.

The general functional form for time as a function of distance and local angle α is given by:

$$t(x, \alpha) = ax + bx^3 + cx^3 + d_\alpha x^4. \quad (4)$$

8.1.7. Dependence of Distance-to-Time Function on Magnetic Field Strength

Since the R2 chambers are located within the field region of the CLAS12 torus, the magnetic field affects the drift velocity as shown in Fig. 20b. In particular, the field rotates and shrinks the isochrones as shown in Fig. 19b. These effects can be modeled by a modification to the effective entrance angle of the track and by an increase in the time at a particular DOCA. Both of these corrections are assumed to depend only on the magnitude of the magnetic field, and not its direction, following a study described in Ref. [21].

The rotation of the isochrones is parameterized as a shift in the effective entrance angle as:

$$\alpha_b = \alpha_0 + \cos^{-1}(1 - b_{rot}B), \quad (5)$$

where α_0 is the actual entrance angle, b_{rot} is a parameter equal to 0.02°/T, and B is the magnetic field strength in Tesla.

The drift isochrones are not only rotated but are shrunk by a non-zero magnetic field. The drift time was parameterized as:

$$t(B) = t(0) + b_{mag}B^2, \quad (6)$$

where b_{mag} is an adjustable parameter that is determined by calibration with a value of approximately 100 ns/T^2 and B is the magnetic field strength in Tesla. In this expression, the first term is the time calculated assuming B=0, and the second term is the time increase due to the B field. For the R1 and R3 functions, no magnetic field dependence is included, as the chambers are located outside the torus cryostats in regions where field strengths are less than 0.2 T. See Ref. [22] for a related parameterization of the change in the distance at a particular time due to a magnetic field.

8.2. Calibrating the Distance-to-Time Function Parameters

Each hit on a track is characterized by two parameters, the measured drift time from the sense wire and the distance-of-closest-approach (TRKDOCA) to the sense wire. A best fit to the dependence of time on TRKDOCA determines the values of the parameters of the drift-velocity function. We determine the optimized values of these function parameters by fitting a histogram of TRKDOCA vs. time, storing the fit parameters in a database, re-doing the track fitting, and iterating.

To illustrate our fits, in Fig. 21 we show a plot of the data (time vs. TRKDOCA) and over-plotted is the function (time vs. DOCA). The function does a fair job of following the shape of the data.

8.2.1. Using the Distance-to-Time Function in Reconstruction

The track reconstruction program needs to know the expected distance as a function of time. However, as explained in the previous section, we have calibrated and fit the observed time as a function of distance. So, we numerically invert the $t = f(x)$ function in order to fill a table of x (real number) as a function of the time index (integer).

This means that we:

- Fill our time-to-distance tables for different local angles using the function;
- Interpolate between time-to-distance tables for different local angles to obtain the calculated distance at a particular local angle;
- For R2, interpolate between different B-field tables.

We interpolate between different local angle tables linearly in $\cos(30^\circ - \alpha)$. For example if "X_0" is the distance (at a particular time) for a table filled for tracks with local angle of 0° and "X_{30}" is the corresponding quantity for a table of 30° tracks, then

$$X(t, \alpha) = X_0 + (X_{30} - X_0)\frac{\cos(30^\circ - \alpha) - \cos(30^\circ)}{\cos(0^\circ) - \cos(30^\circ)}. \quad (7)$$

We interpolate between different B-field tables linearly in B^2.

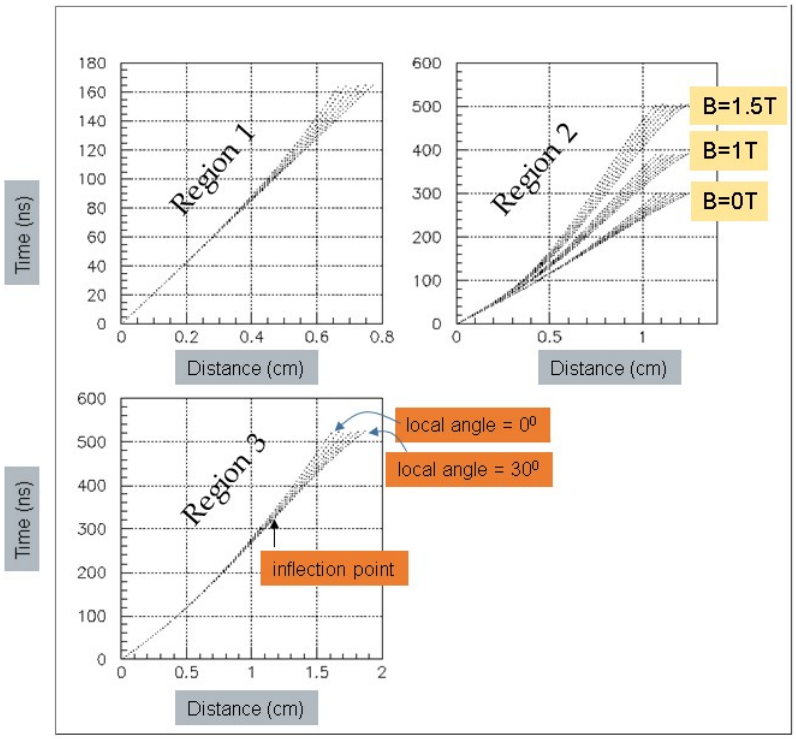

Figure 20: Scatterplot of the corrected drift time vs. TRKDOCA for (upper left) R1, showing curves for various local angles from 30° (right-most curve) to 0° (left-most curve). (Upper right) for R2; additionally showing 3 bands for B-field magnitudes of 0, 1, 1.5 T. (Lower left) for R3 with the inflection point identified.

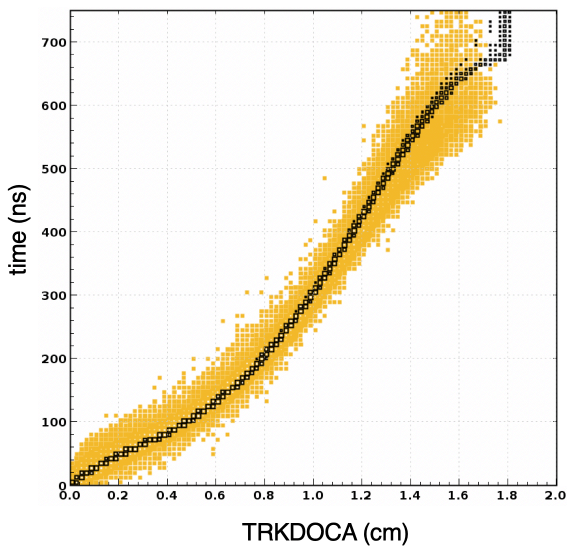

Figure 21: A plot of time vs. TRKDOCA from our track fits. Over-plotted in darker symbols is the calculated distance (DOCA) vs. time.

8.3. Alignment Procedures and Corrections for Geometrical Distortions

Each of the 18 drift chambers was surveyed with millimeter to sub-millimeter accuracy, but we wanted an independent check of the chambers' positions and we needed to know the absolute position to about 0.05 mm in order to achieve momentum resolutions on the order of 0.3%, which was a goal beyond our initial specifications that we thought achievable. For these reasons, the survey values for the chamber geometry were viewed only as a reasonable starting point to be refined by comparisons with data.

To adjust the chamber geometry parameters we analyzed "straight-track" data taken with both magnets (torus and solenoid) turned off. Tracks were found and fitted with our standard track reconstruction [23] package. For various bins in the angle of the track, we measured the shifts of the track residual means as a function of layer number. Before correcting for misalignment in software, the data showed significant displacements of the means from zero, as large as 2 mm; see Fig. 22.

To analyze the data we used the concept of simulating trial residual distributions by deliberately misaligning the chambers. On a first pass through the data we used misalignment parameters (shifts and rotations of individual chambers) set to zero. On subsequent passes, we deliberately misaligned a particular chamber by a particular offset in position or angle and produced a second set of plots of residual mean vs. layer. We ran 18 passes through the data, adjusting all combinations of Region (1, 2, 3) and of offset type δx, δy, δz, θx, θy, θz, one at a time. The offsets in x, y, and z were 2 mm, and the angular rotations were 0.2°. These 2 mm shifts and 0.2° rotations were called "unit distortions".

We subtracted the pass 1 (nominal) residual distribution from a pass "i" distribution to give a "change of residual" distribution caused by a given "unit distortion". We then fit the observed residual distribution from the data to a weighted sum of the 18 "change of residual" distributions. In principle, we could have had 18 free parameters, but in practice we had 12 free parameters: δx, δy, δz, and θy for each of the 3 chambers: R1, R2, and R3, where θy is a tilt of a chamber. We did not vary the yaw (θx) and roll (θz) degrees of freedom.

Figure 22 plots the mean of the residuals of a straight-line fit to the tracks vs. layer (1 - 36 layers of the chambers) for all six sectors. The misalignment is plainly visible as a noticeable shift of the residual means from zero. The bulk of the offsets occurs in shifts of groups of 12 layers, which corresponds to one physical chamber (a R1 chamber has layers 1-12, R2 from 13-24, and R3 from 25-36). The RMS deviations of the means from zero average to about 50 μm.

Because our "unit distortions" are not orthogonal functions, we needed to do a simultaneous fit over four angular ranges because two "unit distortions", which are highly correlated in one angular range, were usually not in other ranges.

The alignment procedure described so far considered only the relative alignment of the three drift chambers in any particular sector to each other. Our only inter-sector constraint was that all sectors, after alignment, should point to a common target vertex. In addition to minimizing the residuals from our 36 drift chamber layers, we also include a 37th term in the sum of squared residuals: the distance of closest approach to the beam-target vertex. This requirement, that all tracks, regardless of sector, should point to a common beam-target vertex, allowed us to align the chambers sector to sector.

The results of this procedure indicated that the best-fit position of the chambers along the three coordinate axes varied by up to several millimeters relative to the surveyed positions. Our best estimate of the final average offset of the chambers after alignment was approximately 65 μm.

8.3.1. Geometrical Distortions

The drift chamber internal geometry (placement of wires, etc.) was checked by detailed surveys of the endplate, and of the endplate positions with respect to the survey holes located on the noseplate and backplate during construction of the full chamber assembly and before stringing. As discussed in the previous section, we surveyed the chambers into place on the torus and also applied a "straight-track" analysis to fine-tune our knowledge of each chamber's geometrical location and orientation.

In addition to these alignment procedures, which treat each chamber as a rigid, fixed geometrical shape, we also measured and corrected two important chamber distortions: wire sagging due to gravity and bowing inward of the endplates in response to the collective wire tension.

The wire sag can be a large as 1 mm for our 4 m long wires. For this small sag, it is sufficient to describe the shape of the sag as a parabola with maximum deviation from a straight line occurring at the midplane of the chamber. This correction to the hit position can be applied at "event time" when the hit position along the wire has been determined.

The second type of geometrical distortion is due to the bowing of the endplates. Because we wished to keep the endplates as thin as possible and because we did not wish to obstruct the active area of the chamber volume with material, the entire tension load was borne by the endplates, which had a simple support at the small noseplate and a fixed support at the backplate.

We did extensive engineering analysis and also post-stringing surveys to determine the size and pattern of this bowing. Because our endplate planes are not perpendicular to the wires, when they bow they move the wire endpoints radially outward and along the wire direction. The amount varies according to the chamber position because the weight of the endplates also plays a role, but the bowing in the direction perpendicular to the wire could be as large as 1.5 mm. This point of maximum deflection occurs about a fourth of the way between the

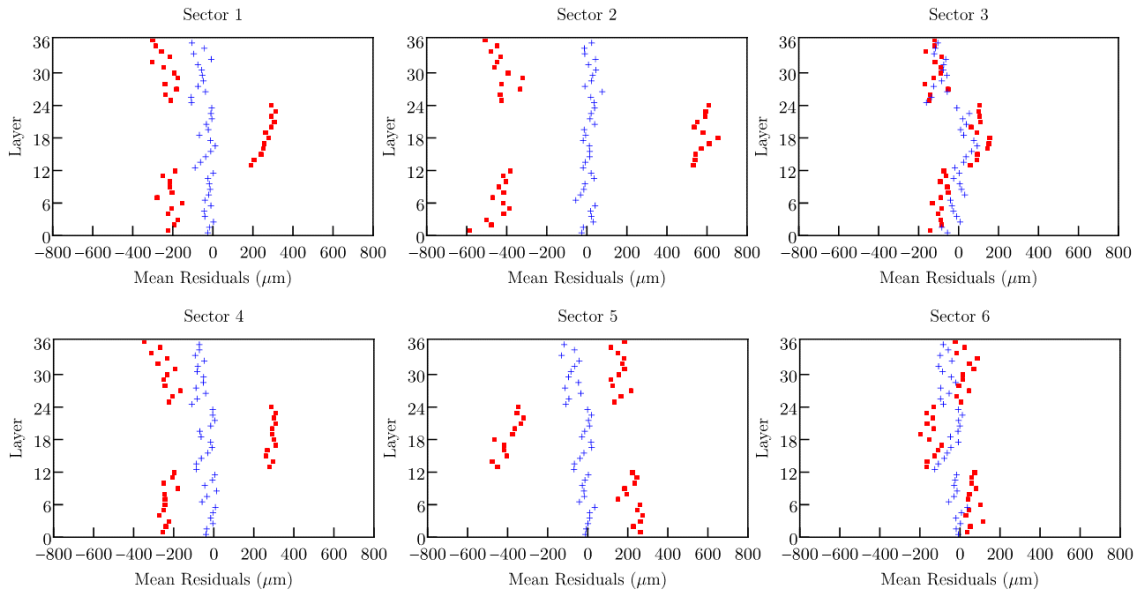

Figure 22: Plots of the fit residual mean vs. layer, before alignment (red squares) and after alignment (blue crosses), for each of the six sectors. The displacements occur in correlated groups, layers (1-12, 13-24, and 25-36), which correspond to the three physical chambers, R1, R2, and R3.

noseplate and backplate. In Fig. 23 we show the engineering analysis for a R2 endplate, which agreed well with our direct surveys.

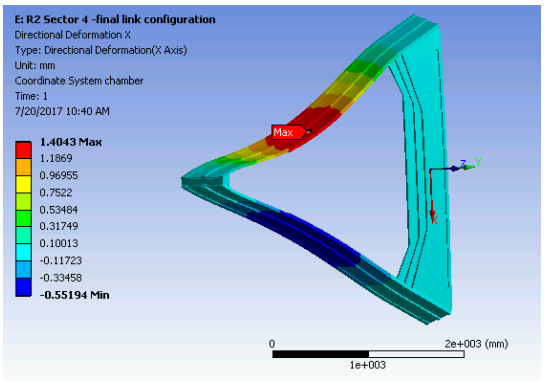

Figure 23: An engineering finite element analysis showing the endplate bowing due to wire tension.

8.4. Magnetic Field Model: A Comparison to Measurement

In the fall of 2016, we mapped the magnetic field of the torus magnet. We documented the equipment and measurements in an article on the construction of the torus (see Ref. [24]) and in internal documents (see Ref. [25]). Further details are also included in Ref. [27].

We used three independent 1-dimensional Hall probes mounted in a precision-machined Teflon holder. The holder was a cylindrical solid that was moved in 5-cm increments by a precision stepper motor and screw assembly down a precision carbon-fiber tube. The probes were precisely spaced to be 5 cm apart in the z-dimension (along the beamline), with one oriented perpendicular to the z-axis, another perpendicular to the y-axis (vertical), and the third perpendicular to the x-axis (horizontal). In this way, we measured the x, y, and z components of the magnetic field at z-points separated by 5 cm along the axis of the toroid.

The carbon-fiber tube was positioned in x and y by precision-machined positioning plates at the upstream and downstream ends of the torus. There were 24 precise hole locations on each plate (4 between each pair of torus coils). Of the 4 holes in any one of the six sectors, one was midway between coils at 30 cm radius ("Hole A"), one midway at 46.5 cm radius ("Hole C"), and the two others ("Holes B and D") at 46.5 cm radius but displaced azimuthally by $\pm 15°$ away from the sector midplane. In total, we measured B_x, B_y, B_z at 40 locations in z at each of the 24 (x, y) locations,

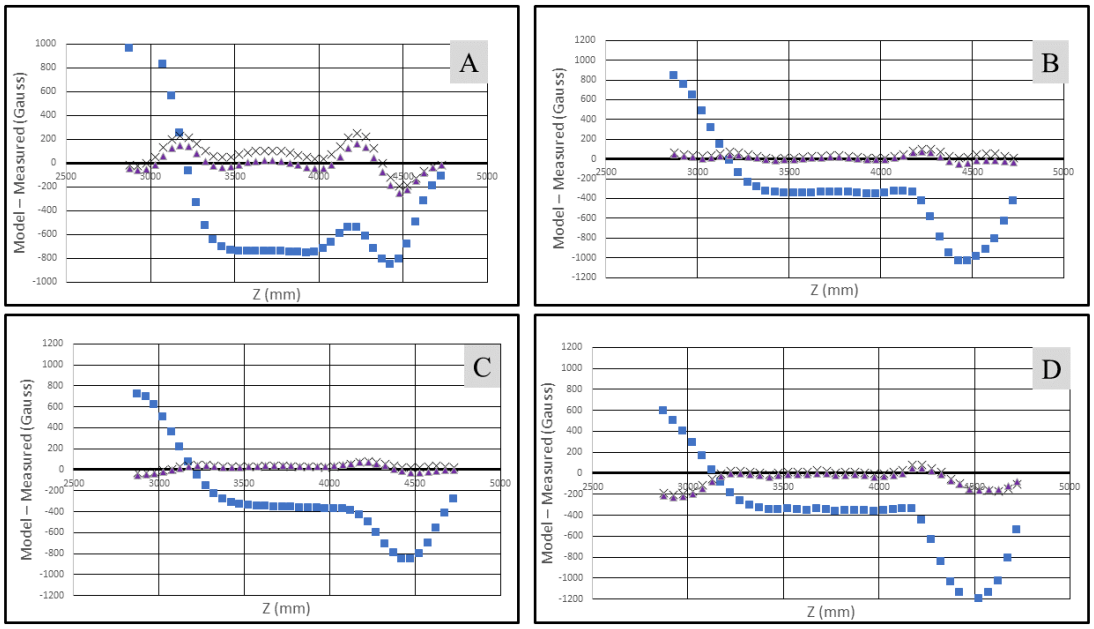

Figure 24: A plot of Bmodel - Bmeasured (in Gauss) vs. z (mm) for the 160 measurement points within one sector (Sector 1) of the torus magnet. Sub-figure A corresponds to measurements at a radius of 30 cm and a ϕ of 0° (on the midplane). Sub-figures B, C, and D are for measurements taken at a radius of 46.5 cm and at ϕ values of -15°, 0°, and 15°, respectively.

resulting in 2880 measurements.

By adjusting the six coils' shapes and locations, we were able to match our magnetic model to the measurements to an accuracy of 0.5%. Details of this analysis will be available in a future publication, but in summary we show in Fig. 24 the difference between the magnetic field from our models (in Gauss) and the measured value for the 160 measurements taken in one of the sectors between two coils. The measurements in sub-figure A were taken at a radius of 30 cm, which is the region of the highest magnetic field (∼2 T) and is most important for our low-angle, high-momentum tracks. Sub-figures B, C, and D are measurements taken at a radius of 46.5 cm.

The (measured-modeled) value is shown for 3 models: our original model (blue squares), our first adjusted model in which the average coil shape is modified but each coil is in its ideal location (black X's), and our latest model (purple triangles) in which each coil has the same, modified shape but individual coil positions are adjusted to give the best agreement with the measurements. At this time, the average fractional difference between model and measurement is about 0.5%.

9. Drift Chamber Tracking System Performance

In this section, we describe the tracking system performance: the ability to operate at high luminosity, the efficiency at reconstructing charged particle tracks, and the spatial resolution of such tracks.

9.1. Operation at High Luminosity

In order to satisfy the statistical requirements of the experimental program, an important design goal for CLAS12 is the ability to make routine measurements with electron beam luminosities up to 10^{35} cm^{-2}s^{-1}. The luminosity limit in CLAS12 is set by the large flux of Møller electrons and low-energy photons produced from the targets by the multi-GeV incident electron beam. This constraint is severe for the drift chambers since they are close to the target.

Particularly for the R1 chambers, the large flux of particles limits the luminosity in several ways. First, the chambers must be able to operate with an acceptably low trip rate. Second, the accidental occupancy in the chambers should be on the order

of 5% or less in order to keep the track-finding inefficiencies at a moderate level. See the accompanying article on track reconstruction ([23]) for a quantitative discussion of this effect. Third, the effects of sustained high luminosities can be unfavorable for long chamber lifetimes. Aging correlates directly with the currents generated in the chambers. However, our choice of an argon-CO_2 gas mixture and strict control of materials in contact with the gas should provide a long chamber lifetime. For the previous CLAS chambers, we used the same gas mixture and ran at a similar gain and similar currents, and the chambers operated for more than 10 years with no indication of aging. We expect the present chambers to perform well for at least 10 years.

9.2. Tracking Inefficiency: Intrinsic, Malfunction-Related, and Background-Related

The probability of not reconstructing a charged particle track due to a charged particle within our fiducial volume is referred to as the "tracking inefficiency". The tracking inefficiency has three root causes:

1. intrinsic layer inefficiency: the failure to record a hit for a track crossing a layer, when all wires and electronics are operating properly;
2. malfunction-related inefficiency: loss of hits and sometimes whole track segments because of equipment malfunctions;
3. background-related inefficiency: out-of-time background can interfere with the segment-finding algorithms when a background-related track segment lies "on top" of a real, in-time, segment.

9.2.1. Simulation of Inefficiencies

In our generation and reconstruction of simulated events, we estimate the size of the three types of inefficiency in the following manner:

1. simulation of intrinsic layer inefficiency: this is a random process and, as such, it is handled at event generation time by our Geant4 Monte Carlo simulation program GEMC [26]. For each superlayer (1-6), we have defined a DOCA-dependent layer inefficiency function, as determined from the data. At hit-generation time in GEMC a random number (between 0 and 1) is generated, and if it is smaller than the layer inefficiency function, the hit is not digitized.
2. simulation of malfunction-related inefficiency: the GEMC Monte Carlo hits are generated as if there are no malfunctions of the wires. During the Monte Carlo reconstruction, however, a status table for each hit wire is queried and if the wire is in the "bad status" list, that hit is not used in the tracking. The malfunction-related inefficiency is small. At this time, roughly 0.5% of our wires are not operating properly.
3. simulation of background-related inefficiency: rather than try to simulate out-of-time background due to all physics processes, we merge "random-trigger" events with events from low-luminosity runs and compare the efficiency of these merged events with that from un-merged low-luminosity events. This ratio is considered to be a measure of the background-related inefficiency.

We will not further discuss the malfunction-related inefficiency or the background-related inefficiency further in this article. See our companion article on track reconstruction for more details [23]. Here we present our results on measuring the intrinsic layer inefficiency.

9.2.2. Intrinsic Layer Inefficiency

The layer inefficiency is the probability that a good hit is not recorded in a wire layer through which the track has passed, based on the evidence from all other layers in the superlayer. This is called the "excluded-layer method". The layer inefficiency is a measure of the intrinsic drift cell inefficiency for the particular choice of gas mixture, high voltage set point, and discriminator level.

The single layer inefficiency is not uniform across the drift cell. It is slightly higher near the sense wire and substantially higher near the outer edge of the cell. A track passing close to a sense wire leaves many ions in the cell, but the ion arrival times are stretched out from near-zero to the maximum drift time $Tmax$. The result is that the preamplifier's output signal has a low voltage amplitude but persists for a long time. So, even though the collected charge is large, the output signal of our transimpedance preamplifiers may not be large enough to exceed the voltage discriminator threshold of the DCRB. For the case of tracks near the outer edge of the cell (so-called "corner-clippers"), they leave a very small number of ions in the cell and thus have a small signal.

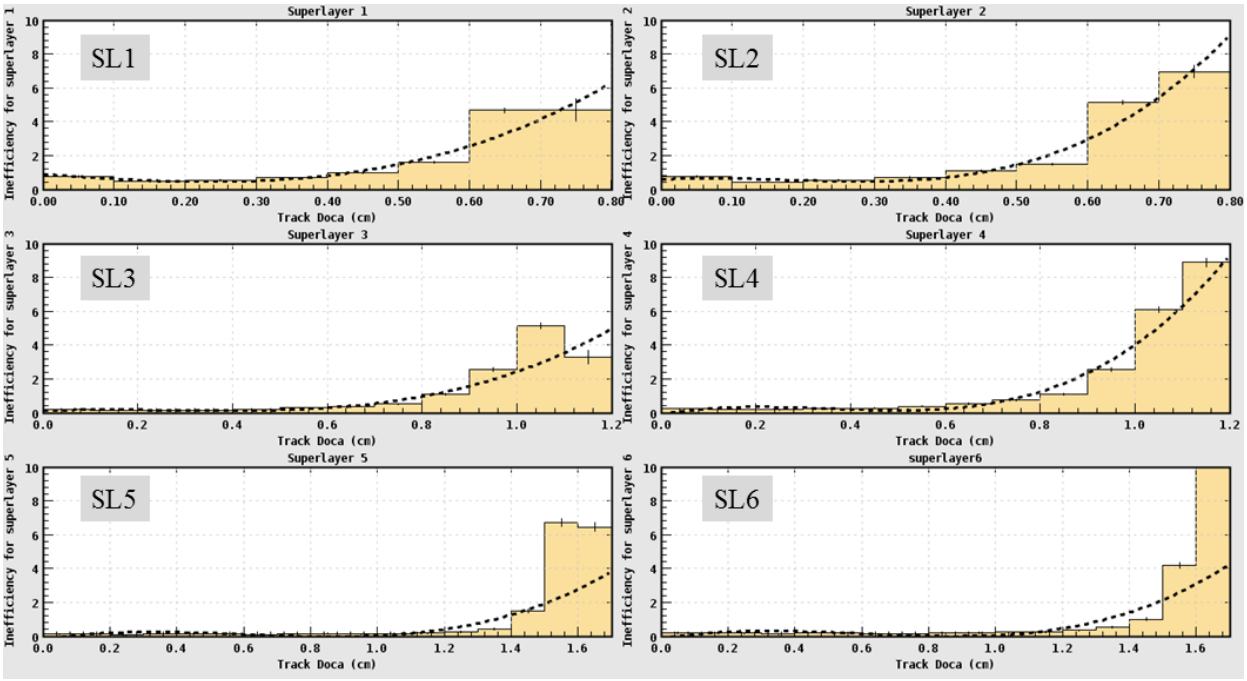

Figure 25: The observed layer inefficiency as a function of DOCA. Hits from tracks that pass close to or far from the sense wire have their signals spread out in time, and the resulting voltage pulse from the preamplifiers may fail to cross the discriminator threshold, resulting in a "lost hit".

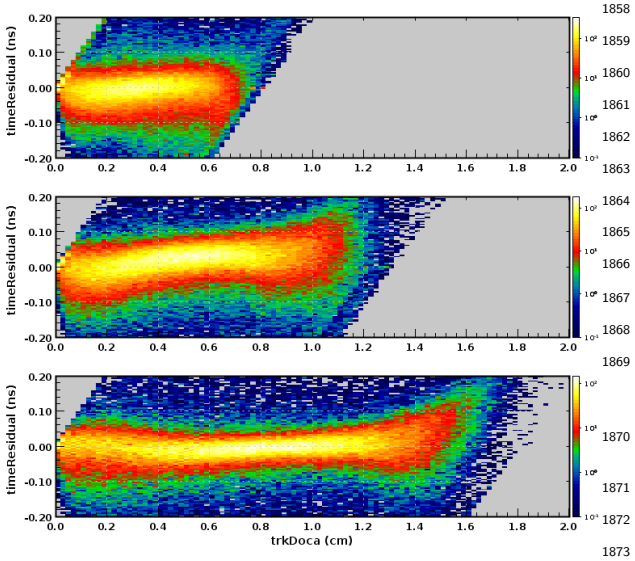

Figure 26: The hit resolution plotted vs. TRKDOCA for R1, R2, and R3 (top, middle, bottom), respectively.

Figure 25 shows that the largest contribution to the drift cell inefficiency is from tracks far from the wire. These tracks may leave very few ions. Even tracks that are far from the wire but leave a substantial number of ions can give rise to inefficiencies due to a large spread in ion arrival time. These tracks produce signals that have low pulse height and long duration, and thus may escape detection. We fit this observed DOCA-dependent inefficiency to a functional form that is used in our GEMC Monte Carlo hit digitization routine to randomly throw out this percentage of hits.

The average layer efficiency of all wires (excluding the 0.5% of malfunctioning wires) is greater than 98%.

9.3. Drift Chamber Spatial Resolution

The single-wire resolution is the RMS spread of the difference between the fit TRKDOCA of the track and the value of DOCA as calculated from the time of the hit. The variance of this residual distribution is the quadratic sum of the single-wire resolution and the track position uncertainty. This variance over-estimates the single-wire resolution. Since there are six layers per superlayer, this amounts to a $10-15\%$ over-estimate.

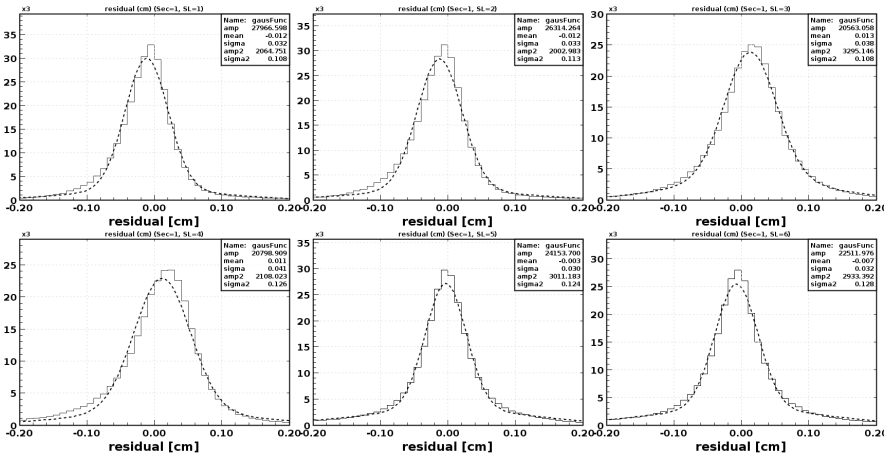

Figure 27: A plot of the residual distributions for all 6 superlayers in Sector 1. Over-plotted is a double-Gaussian fit to the distribution.

Figure 26 shows the width of the track-hit residual distribution plotted vs. TRKDOCA for each of the different chamber regions. The single-wire resolution worsens near the wire and also at the outer edge of the cell. This arises due to finite cluster sizes due to the Poisson distribution of ion-pair production along the path of the primary ion near the sense wire along with time-walk effects and the divergent nature of the electric field lines near the field wire.

A more quantitative look at the resolution is given in Fig. 27. This is a plot of the residual distributions from each of the six superlayers in Sector 1; all sectors have similar results. Because the resolution is narrow in the middle of the cell and widens considerably for small and large values of DOCA (see Fig. 26), we fit the residual distribution to a double-Gaussian form. The average single-wire resolution in the middle portion of the cell is about 325, 395, and 310 μm for R1, R2, and R3, respectively, with a whole cell resolution (RMS) is about 430, 540, and 515 μm for R1, R2, and R3, respectively.

9.4. Summary of Design, Construction, and Operation

The toroidal geometry of the CLAS12 spectrometer necessitated a particle-tracking system of unconventional design. Design challenges and solutions include the following:

- The necessity to conceal inactive areas of the drift chambers within the shadow regions of the torus cryostat resulted in very thin endplates and low-profile wire connection schemes and on-board preamplifiers.
- The toroidal shape of the magnet and the desire to have measurements before, within, and after the high-field region, resulted in the design of a "rod and ball" mounting scheme that minimizes dead areas and facilitates maintenance.
- The fabrication of chambers that support large static wire tensions, but have thin endplates necessitated three endplate designs: aluminum stiffened with steel bars (R1), Stesalit (an epoxy-fiberglass composite) stiffened with steel bars (R2), and thin stainless-steel plates filled with foam and reinforced with carbon-fiber posts on the entrance side and a carbon-foam-carbon composite plate on the exit side (R3).
-The need for precise tracking in a system with non-saturated drift velocity (necessitated by the requirements of large drift distances, non-flammable gas mixtures, and low-gain operation) resulted in a semi-automated calibration and monitoring software package.

9.5. Conclusions

The CLAS12 drift chamber system has been in routine operation since spring, 2017. The system has reached its design goals of operating at high-luminosity (1×10^{35} cm^{-2}s^{-1}) in a high-flux elec-

tromagnetic reaction environment, with very good track reconstruction efficiency over a large range of angles and magnetic fields; see the article on track reconstruction [23]. The percentage of malfunctioning wires, due to high voltage problems, signal connector issues, etc., is presently 0.5%. The single-wire efficiency is greater than 98%.

Calibration efforts are ongoing, and at the time of this publication, the single-wire resolution is about 500 μm averaged over all drift distances and all 18 chambers. The average single-wire resolution in the middle portion of the cell is about 325, 395, and310 μm for R1, R2, and R3, respectively.

Acknowledgments

The authors wish to thank the crews of wire stringers and technicians who participated during the chamber construction at Idaho State University, Old Dominion University, and Jefferson Laboratory, as well as the support of the technicians involved with installation of the detectors into CLAS12. This material is based upon work supported by the U.S. Department of Energy, Office of Science, Office of Nuclear Physics under contract DE-AC05-06OR23177, as well as by DOE grants DE-FG02-87ER40315, DE-FG05-94ER40859, DE-FG02-96ER40960, DE-FG02-96ER40980, and NSF grant NSF-PHY-9412479.

References

[1] V.D. Burkert *et al.*, *"The CLAS12 Spectrometer at Jefferson Laboratory"*, to be published in Nucl. Inst. and Meth. A, (2020). (see this issue)

[2] B.A. Mecking *et al.*, Nucl. Inst. and Methods A **503**, (2003) 513-553.

[3] M.D. Mestayer *et al.*, Nucl. Inst. and Methods A **449**, (2000) 81-111.

[4] J.A. Kadyk, Nucl. Inst. and Methods A **300**, 436 (1991).

[5] W. Campbell and J. Scialdone, "Outgassing Data for Selecting Spacecraft Materials", NASA internal report RP-1124 Rev. 3 (1993).

[6] S.B. Christo, "Considerations for Crimping the CLAS Drift Chamber Wires", CLAS-Note 89-021, (1989). https://www.jlab.org/Hall-B/notes/clas_notes89/note89-021.pdf

[7] S.B. Christo and M.D. Mestayer, "Minimizing Cathode Emission in Drift Chambers", CLAS-Note 92-016, (1992). https://www.jlab.org/Hall-B/notes/clas_notes92/92-016.pdf

[8] U.S. Patent 8,863,568 "Apparatus and procedure to characterize the surface quality of conductors by measuring the rate of cathode emission as a function of surface electric field strength", Mac Mestayer, Steve Christo, and Mark Taylor.

[9] S. Bernreuther *et al.*, Nucl. Inst. and Methods A **367**, 96 (1995); W.L. Imhof *et al.*, Space Science Reviews **71**, 305 (1995).

[10] R. Bouclier *et al.*, Nucl. Inst. and Methods A **350**, 464 (1994).

[11] F.J. Barbosa, "A Preamp for the CLAS DC", CLAS-Note 92-003, (1992). https://www.jlab.org/Hall-B/notes/clas_notes92/note92-003.pdf

[12] S. Boyarinov *et al.*, *"The CLAS12 Data Acquisition System"*, to be published in Nucl. Inst. and Meth. A, (2020). (see this issue)

[13] B. Raydo *et al.*, *"The CLAS12 Trigger System"*, to be published in Nucl. Inst. and Meth. A, (2020). (see this issue)

[14] Y. Chiba *et al.*, Nucl. Inst. and Methods A **269**, 171 (1988).

[15] L. Malter, Phys. Rev. 50, 48 - 58 (1936).

[16] M.D. Mestayer, "Choosing the Correct Combination of Sense, Field, and Guard Wire Voltage", CLAS-Note 92-005, (1992). https://www.jlab.org/Hall-B/notes/clas_notes92/note92-005.pdf

[17] GARFIELD has been developed at the University of Mainz by R. Veenhof and revised by M. Guckes and K. Peters. See HELIOS-Note 154, (1986).

[18] D.S. Carman *et al.*, *"The CLAS12 Forward Time-of-Flight System"*, to be published in Nucl. Inst. and Meth. A, (2020). (see this issue)

[19] M.D. Mestayer *et al.*, Nucl. Inst. and Methods A **367**, 316 (1995).

[20] T. Zhao *et al.*, Nucl. Inst. and Methods A **340**, (1994) 485-490.

[21] M.D. Mestayer *et al.*, IEEE Transactions on Nuclear Science **39** No. 4, 690 (1992).

[22] L.M. Qin *et al.*, "Performance of a Region II Drift Chamber Prototype and Region II Drift Chamber Tracking", CLAS-Note 96-018, (1996). https://www.jlab.org/Hall-B/notes/clas_notes96/note96-018.ps.gz

[23] V. Ziegler *et al.*, *"The CLAS12 Software Framework and Event Reconstruction"*, to be published in Nucl. Inst. and Meth. A, (2020). (see this issue)

[24] Probir K. Ghoshal *et al.*, IEEE Transaction on Applied Superconductivity, Vol. 29, No. 4, June 2019.

[25] J. Newton *et al.* "Measuring and Modelling the CLAS12 Torus Magnetic Field", CLAS12-Note (to be written)

[26] M. Ungaro *et al.*, *"The CLAS12 Geant4 Simulation"*, to be published in Nucl. Inst. and Meth. A, (2020). (see this issue)

[27] R. Fair *et al.*, *"The CLAS12 Superconducting Magnets"*, to be published in Nucl. Inst. and Meth. A, (2020). (see this issue)